SPECTROSCOPIC OBSERVATIONS OF SN 2012fr: A LUMINOUS, NORMAL TYPE Ia SUPERNOVA WITH EARLY HIGH-VELOCITY FEATURES AND A LATE VELOCITY PLATEAU

M. J. Childress[1,2], R. A. Scalzo[1,2], S. A. Sim[1,2,3], B. E. Tucker[1], F. Yuan[1,2], B. P. Schmidt[1,2], S. B. Cenko[4],
J. M. Silverman[5], C. Contreras[6], E. Y. Hsiao[6], M. Phillips[6], N. Morrell[6], S. W. Jha[7], C. McCully[7], A. V. Filippenko[4],
J. P. Anderson[8], S. Benetti[9], F. Bufano[10], T. de Jaeger[8], F. Forster[8], A. Gal-Yam[11], L. Le Guillou[12], K. Maguire[13],
J. Maund[3], P. A. Mazzali[9,14,15], G. Pignata[10], S. Smartt[3], J. Spyromilio[16], M. Sullivan[17], F. Taddia[18], S. Valenti[19,20],
D. D. R. Bayliss[1], M. Bessell[1], G. A. Blanc[21], D. J. Carson[22], K. I. Clubb[4], C. de Burgh-Day[23], T. D. Desjardins[24],
J. J. Fang[25], O. D. Fox[4], E. L. Gates[25], I.-T. Ho[26], S. Keller[1], P. L. Kelly[4], C. Lidman[27], N. S. Loaring[28], J. R. Mould[29],
M. Owers[27], S. Ozbilgen[23], L. Pei[22], T. Pickering[28], M. B. Pracy[30], J. A. Rich[21], B. E. Schaefer[31], N. Scott[29],
M. Stritzinger[32], F. P. A. Vogt[1], and G. Zhou[1]

[1] Research School of Astronomy and Astrophysics, Australian National University, Canberra, ACT 2611, Australia; mjc@mso.anu.edu.au
[2] ARC Centre of Excellence for All-sky Astrophysics (CAASTRO)
[3] Astrophysics Research Centre, School of Mathematics and Physics, Queen's University Belfast, Belfast BT7 1NN, UK
[4] Department of Astronomy, University of California, Berkeley, CA 94720-3411, USA
[5] Department of Astronomy, University of Texas, Austin, TX 78712-0259, USA
[6] Las Campanas Observatory, Carnegie Observatories, Casilla 601, La Serena, Chile
[7] Department of Physics and Astronomy, Rutgers, the State University of New Jersey, 136 Frelinghuysen Road, Piscataway, NJ 08854, USA
[8] Departamento de Astronomía, Universidad de Chile, Casilla 36-D, Santiago, Chile
[9] INAF Osservatorio Astronomico di Padova, Vicolo dell'Osservatorio 5, I-35122 Padova, Italy
[10] Departamento de Ciencias Fisicas, Universidad Andres Bello, Avda. Republica 252, Santiago, Chile
[11] Department of Particle Physics and Astrophysics, The Weizmann Institute of Science, Rehovot 76100, Israel
[12] UPMC Univ. Paris 06, UMR 7585, Laboratoire de Physique Nucleaire et des Hautes Energies (LPNHE), F-75005 Paris, France
[13] Department of Physics (Astrophysics), University of Oxford, DWB, Keble Road, Oxford OX1 3RH, UK
[14] Astrophysics Research Institute, Liverpool John Moores University, Egerton Wharf, Birkenhead CH41 1LD, UK
[15] Max-Planck-Institut für Astrophysik, Karl-Schwarzschild-Strasse 1, D-85748 Garching, Germany
[16] European Southern Observatory, Karl-Schwarzschild-Strasse 2, D-85748 Garching, Germany
[17] School of Physics and Astronomy, University of Southampton, Southampton SO17 1BJ, UK
[18] The Oskar Klein Centre, Department of Astronomy, AlbaNova, Stockholm University, SE-10691 Stockholm, Sweden
[19] Las Cumbres Observatory Global Telescope Network, 6740 Cortona Drive, Suite 102, Goleta, CA 93117, USA
[20] Department of Physics, University of California, Broida Hall, Mail Code 9530, Santa Barbara, CA 93106-9530, USA
[21] Observatories of the Carnegie Institution of Washington, 813 Santa Barbara Street, Pasadena, CA 91101, USA
[22] Department of Physics and Astronomy, University of California, Irvine, CA 92697-4575, USA
[23] School of Physics, University of Melbourne, Parkville, VIC 3010, Australia
[24] Department of Physics and Astronomy, The University of Western Ontario, London, ON N6A 3K7, Canada
[25] University of California Observatories/Lick Observatory, University of California, Santa Cruz, CA 95064, USA
[26] Institute for Astronomy, University of Hawaii, 2680 Woodlawn Drive, Honolulu, HI 96822, USA
[27] Australian Astronomical Observatory, P.O. Box 915, North Ryde, NSW 1670, Australia
[28] South African Astronomical Observatory (SAAO), P.O. Box 9, Observatory 7935, South Africa
[29] Centre for Astrophysics & Supercomputing, Swinburne University of Technology, P.O. Box 218, Hawthorn, VIC 3122, Australia
[30] Sydney Institute for Astronomy, School of Physics, University of Sydney, NSW 2006, Australia
[31] Department of Physics and Astronomy, Louisiana State University, Baton Rouge, LA 70803, USA
[32] Department of Physics and Astronomy, Aarhus University, Ny Munkegade 120, DK-8000 Aarhus C, Denmark

ABSTRACT

We present 65 optical spectra of the Type Ia SN 2012fr, 33 of which were obtained before maximum light. At early times, SN 2012fr shows clear evidence of a high-velocity feature (HVF) in the Si II $\lambda6355$ line that can be cleanly decoupled from the lower velocity "photospheric" component. This Si II $\lambda6355$ HVF fades by phase -5; subsequently, the photospheric component exhibits a very narrow velocity width and remains at a nearly constant velocity of $\sim$12,000 km s^{-1} until at least five weeks after maximum brightness. The Ca II infrared triplet exhibits similar evidence for both a photospheric component at $v \approx 12{,}000$ km s^{-1} with narrow line width and long velocity plateau, as well as an HVF beginning at $v \approx 31{,}000$ km s^{-1} two weeks before maximum. SN 2012fr resides on the border between the "shallow silicon" and "core-normal" subclasses in the Branch et al. classification scheme, and on the border between normal and high-velocity Type Ia supernovae (SNe Ia) in the Wang et al. system. Though it is a clear member of the "low velocity gradient" group of SNe Ia and exhibits a very slow light-curve decline, it shows key dissimilarities with the overluminous SN 1991T or SN 1999aa subclasses of SNe Ia. SN 2012fr represents a well-observed SN Ia at the luminous end of the normal SN Ia distribution and a key transitional event between nominal spectroscopic subclasses of SNe Ia.

Key words: galaxies: individual (NGC 1365) – supernovae: general – supernovae: individual (SN 2012fr)

Online-only material: color figures

1. INTRODUCTION

Type Ia supernovae (SNe Ia) are critical cosmological tools for measuring the expansion history of the universe (Riess et al. 1998; Perlmutter et al. 1999), yet much remains unknown about the nature of these enlightening explosions. Their luminosities show low intrinsic dispersion ($\sim$0.35 mag) and they generally obey a scaling of their absolute luminosity with the width of their optical light curve (Phillips 1993; Phillips et al. 1999) about which the brightness dispersion is even lower. The width–luminosity relationship appears to be driven by the amount of radioactive ^{56}Ni produced in the explosion and the opacity (Hoeflich & Khokhlov 1996; Pinto & Eastman 2000; Mazzali et al. 2001, 2007), but the progenitor mechanism driving these properties remains uncertain. While it is generally accepted that SNe Ia arise from the thermonuclear disruption of a carbon–oxygen (C–O) white dwarf (WD) in a binary system (Hoyle & Fowler 1960), scenarios in which the companion is a main sequence or red giant star (the single-degenerate scenario; Whelan & Iben 1973) and those in which the companion is another WD (the double-degenerate scenario; Tutukov & Iungelson 1976; Tutukov & Yungelson 1979; Iben & Tutukov 1984; Webbink 1984) have both proven consistent with some observational features of SNe Ia. Whether SNe Ia represent a unified class of objects with a common physical origin or result from multiple progenitor channels has yet to be determined, and is a critical question for the continued use of SNe Ia in cosmology.

Optical spectroscopy of SNe Ia can provide vital insight into the question of SN Ia diversity. Large samples of SN Ia spectra have been made publicly available (e.g., Matheson et al. 2008; Blondin et al. 2012; Silverman et al. 2012a; Yaron & Gal-Yam 2012), and investigations of spectroscopic subclassification of SNe Ia have been a vigorous area of study (Benetti et al. 2005; Branch et al. 2009; Wang et al. 2009a; Silverman et al. 2012c). While a rigorous accounting of the diversity of SNe Ia is crucial for understanding the source of their luminosity dispersion, individual cases of well-studied SNe Ia (e.g., Stanishev et al. 2007; Wang et al. 2009b; Foley et al. 2012; Silverman et al. 2012b) can yield key insights into the nature of the explosions themselves.

In this work, we focus on optical spectroscopy of SN 2012fr, an SN Ia which was discovered on 2012 October 27 in the nearby barred spiral galaxy NGC 1365. Shortly after its discovery, we initiated a rigorous photometric and spectroscopic follow-up program for SN 2012fr. Optical photometry will be presented by C. Contreras et al. (2013, in preparation, hereafter Paper II), where we show that SN 2012fr has a normal light curve for an SN Ia. This paper presents optical spectra of SN 2012fr, while E. Y. Hsiao et al. (2013, in preparation, Paper III) will present near-infrared (NIR) spectra and B. Tucker et al. (2013, in preparation Paper IV) will analyze constraints on the progenitor from pre-explosion imaging and very early photometry.

This paper is organized as follows. In Section 2, we present the observational data. Section 3 focuses on the Si II λ6355 line, and characterizes both the high-velocity features (HVFs) observed at early times and the long velocity plateau observed at late times. Other absorption features of particular note for SN 2012fr—including narrow Na I D, unburned C, the Ca II IR triplet, and Fe-group elements—are inspected in Section 4. We address the spectroscopic "subclassification" of SN 2012fr in the context of modern classification schemes in Section 5. We then discuss implications of our observational results in Section 6 and present concluding remarks in Section 7.

2. SPECTROSCOPIC OBSERVATIONS

SN 2012fr was discovered on 2012 October 27 (UT dates are used throughout this paper) by Klotz et al. (2012) at $\alpha = 03^h33^m36^s.274$, $\delta = -36°07'34''.46$ (J2000) in the nearby barred spiral galaxy NGC 1365, and shortly thereafter classified as an SN Ia (Childress et al. 2012; Buil 2012). Extensive photometric coverage presented in Paper II shows that SN 2012fr reached a peak brightness of $m_B = 12.0$ mag on 2012 November 12.04 with a 15 day decline of $\Delta m_{15}(B) = 0.80$ mag. Given the nominal distance modulus to NGC 1365 of $\mu = 31.3$ mag (Silbermann et al. 1999; Freedman et al. 2001), this implies a peak luminosity of $M_B = -19.3$ mag, placing it in firm agreement with the Phillips (1993) relation.

Spectra of SN 2012fr were collected at multiple locations. The two main sources were the Wide Field Spectrograph (WiFeS; Dopita et al. 2007, 2010) on the Australian National University (ANU) 2.3 m telescope at Siding Spring Observatory in northern New South Wales, Australia, and the Public ESO Spectroscopic Survey of Transient Objects (PESSTO) utilizing the 3.6 m New Technology Telescope (NTT) at La Silla, Chile.

WiFeS spectra were obtained using the B3000 and R3000 gratings, providing wavelength coverage from 3500 Å to 9600 Å with resolutions of 1.5 Å and 2.5 Å (all reported instrument resolutions are full width at half-maximum (FWHM) intensity) in the blue and red channels, respectively. Data cubes for WiFeS observations were produced using the PyWiFeS software[33] (M. J. Childress et al. 2013, in preparation). Spectra of the SN were extracted from final data cubes using a point-spread function (PSF) weighted extraction technique with a simple symmetric Gaussian PSF, and the width of this Gaussian was measured directly from the data cube. We found this method to produce flux measurements consistent with a simple aperture extraction method, but with improved signal-to-noise ratio. Background subtraction was performed by calculating the median background spectrum across all spaxels outside a distance from the SN equal to about three times the seeing disk (which was typically 1''.5–2'' FWHM). Due to the negligible galaxy background and good spatial flat fielding from the PyWiFeS pipeline, this technique produced favorable subtraction of the sky background from the WiFeS spectra of SN 2012fr.

A major component of our observing campaign was a series of optical and NIR spectra obtained as part of the PESSTO (S. Smartt et al. 2013, in preparation)[34] survey using the NTT-3.6 m telescope in La Silla, Chile. Optical spectra from PESSTO were obtained with EFOSC2 (Buzzoni et al. 1984) using the Gr11 and Gr16 grisms, which both have a resolution of 16 Å. NIR spectra were obtained with SOFI (Moorwood et al. 1998) using the GB and GR grisms, which give respective resolutions of 14 Å and 21 Å, with observations dithered to facilitate sky background subtraction. SOFI spectra will be released as part of the PESSTO data products for SN 2012fr, and will constitute a portion of the NIR spectra of SN 2012fr analyzed in Paper III. Both EFOSC and SOFI spectra were reduced using the PESSTO pipeline developed by S. Valenti, which is a custom-built python/pyraf package that performs all standard spectroscopic reduction steps including preprocessing, wavelength and flux calibration, spectrum extraction, and removal of telluric features measured from long-exposure standard-star spectra. Continued observations of SN 2012fr in 2013 are

---

[33] http://www.mso.anu.edu.au/pywifes/
[34] http://www.pessto.org

ongoing as part of the PESSTO operations and will be presented in a future PESSTO paper.

Additional spectra of SN 2012fr were obtained with the Robert Stobie Spectrograph on the South African Large Telescope (SALT), the Grating Spectrograph on the South African Astronomical Observatory (SAAO) 1.9 m telescope, the Kast Double Spectrograph (Miller & Stone 1993) on the Shane 3 m telescope at Lick Observatory, the Wide Field Reimaging CCD Camera (WFCCD) on the 2.5 m Irénée du Pont telescope at Las Campanas Observatory, the Inamori-Magellan Areal Camera and Spectrograph (IMACS; Dressler et al. 2011) on the 6 m Magellan-Baade telescope at Las Campanas, and the Andalucia Faint Object Spectrograph and Camera (ALFOSC) on the 2.5 m Nordic Optical Telescope (NOT) on La Palma.

SALT/RSS observations were obtained with a 900 line mm^{-1} Volume Phased Holographic grating at 3 tilt angles to cover the range 3480–9030 Å. The 1″5 wide slit yielded a resolution of ∼6 Å. Initial processing of the SALT data utilized the SALT science pipeline PySALT[35] (Crawford et al. 2010). SAAO-1.9 m observations used the 300 line mm^{-1} grating (#7) at an angle of 17°5, corresponding to a central wavelength of 5400 Å, a wavelength range of ∼3500–7300 Å, and a resolution of 5 Å. Lick/Kast observations employed the 600 line mm^{-1} grating on the blue arm, blazed at 4310 Å, and provides wavelength coverage of 3500–5600 Å with a resolution of 6–7 Å. Different observers used different gratings on the Kast red arm, including the 300 line mm^{-1} grating blazed at 7500 Å and covering 5500–10,300 Å with a resolution of 11 Å, the 600 line mm^{-1} grating blazed at 7000 Å and covering 5600–8200 Å with 5.5 Å resolution, and the 830 line mm^{-1} grating blazed at 6500 Å and covering 5600–7440 Å with 4 Å resolution. WFCCD observations were obtained with the 400 line mm^{-1} grism yielding 8 Å resolution, and data were reduced following the procedures described in detail by Hamuy et al. (2006). The IMACS spectrum employed the 300 line mm^{-1} grating and 0″9 slit yielding a resolution of 2.7 Å.

All long-slit low-resolution spectra were reduced using standard techniques (e.g., Foley et al. 2003). Routine CCD processing and spectrum extraction were completed with IRAF. We obtained the wavelength scale from low-order polynomial fits to calibration-lamp spectra. Also, we fit a spectrophotometric standard-star spectrum to the data in order to flux calibrate the SN and to remove telluric absorption lines.

We obtained a high-resolution optical spectrum of SN 2012fr with the High Resolution Echelle Spectrometer (HIRES; Vogt et al. 1994) on the 10 m Keck I telescope with the blue cross-disperser ("HIRESb") on 2012 October 29.45. We used the C2 decker (i.e., the 1″15 slit), providing coverage from the atmospheric cutoff to $\lambda = 5960$ Å with a resolution of 37,000.

A full table of our optical spectra is given in Table 1, and a representative plot of our spectral time series is shown in Figure 1. At the earliest epochs of SN 2012fr, our observing strategy was to request spectra from multiple sources worldwide. This resulted in several spectra during the same night (often separated by 0.3–0.5 day) on some occasions, but consistently resulted in at least one spectrum every night until nearly two weeks after maximum light. On nights with extremely poor seeing (>3″) at Siding Spring, some WiFeS observers chose to observe SN 2012fr multiple times due to the inability to observe their own fainter targets. Upon publication of this
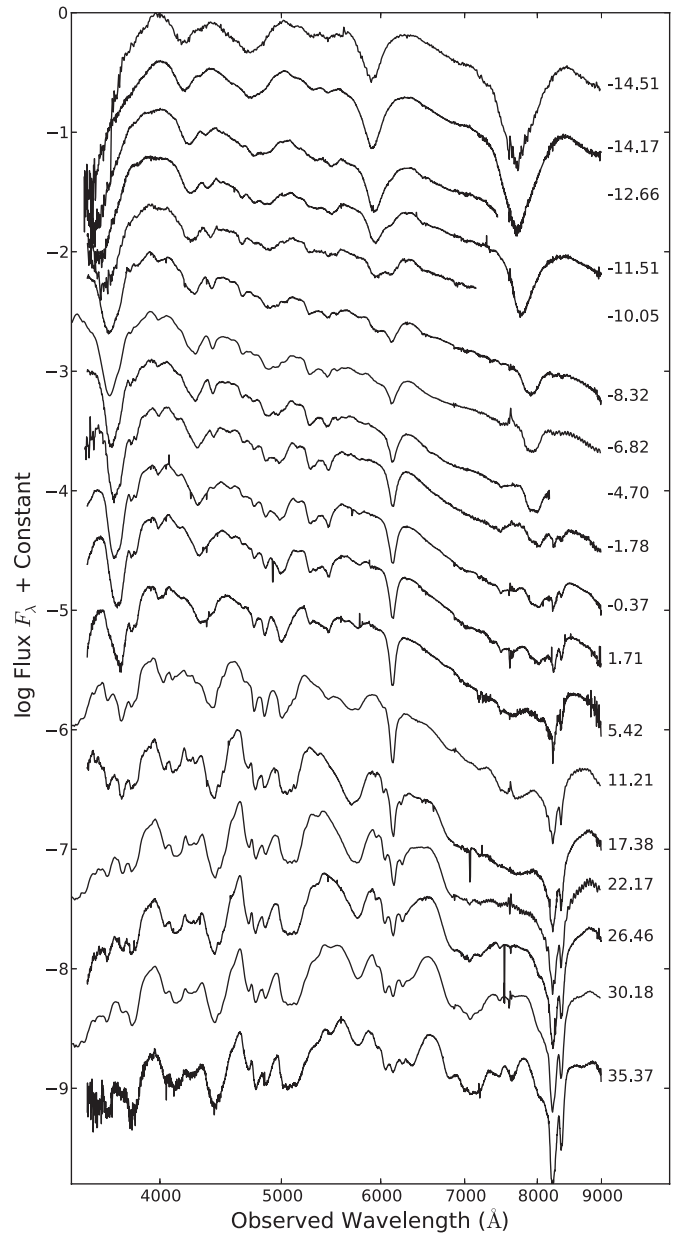
---

[35] http://pysalt.salt.ac.za

Figure 1. Representative sample of SN 2012fr spectra, labeled by phase with respective to *B*-band maximum light.

paper, we will make all of our optical spectra publicly available via the WISEREP (Yaron & Gal-Yam 2012) SN spectroscopy repository.

3. EVOLUTION OF THE S III λ6355 LINE

The Si II λ6355 line is among the most prominent features in SN Ia spectra. Both its characteristics at maximum light (e.g., Nugent et al. 1995) and its evolution in time (e.g., Benetti et al. 2005) have been key tools in characterizing SN Ia diversity. Additionally, the properties of this line in combination with the behavior of other lines ("spectral indicators") have been used to identify potential subclasses of SNe Ia (e.g., Benetti et al. 2005; Bongard et al. 2006; Branch et al. 2009; Silverman et al. 2012c; Blondin et al. 2012).

For SN 2012fr, the evolution of the Si II λ6355 line has three key features of note: (1) the velocity width of the line (and indeed other lines; see Section 4) is extremely narrow, starting about

Table 1
Optical Spectroscopy Observation Log

UT Date	Phase[a] (days)	Telescope/ Instrument	Exposure Time (s)	Wavelength Range (Å)	Observers[b]
2012 Oct 28.53	−14.51	ANU-2.3 m/WiFeS	900	3500–9550	GZ, DB
2012 Oct 28.87	−14.17	SALT/RSS	1200	3480–9030	SJ, CM1
2012 Oct 29.45	−13.59	Keck-I/HIRES	1200	3500–5960	BZ, MJ, SX, BK
2012 Oct 30.38	−12.66	Lick-3 m/Kast	2000	3500–7440	CM2, BZ
2012 Oct 30.51	−12.53	ANU-2.3 m/WiFeS	1200	3500–9550	GZ, DB
2012 Oct 31.53	−11.51	ANU-2.3 m/WiFeS	1200	3500–9550	GZ, DB
2012 Nov 01.59	−10.45	ANU-2.3 m/WiFeS	1200	3500–5700[c]	MB, SK
2012 Nov 01.99	−10.05	SAAO-1.9 m/GS	900	3500–7150	NSL
2012 Nov 02.48	−9.56	ANU-2.3 m/WiFeS	900	3500–9550	MB, SK
2012 Nov 02.69	−9.35	ANU-2.3 m/WiFeS	900	3500–9550	MB, SK
2012 Nov 03.05	−8.99	SAAO-1.9 m/GS	900	3500–7150	NSL
2012 Nov 03.57	−8.47	ANU-2.3 m/WiFeS	900	3500–9550	MB, SK
2012 Nov 03.72	−8.32	ANU-2.3 m/WiFeS	900	3500–9550	MB, SK
2012 Nov 04.07	−7.97	SAAO-1.9 m/GS	900	3500–7150	NSL
2012 Nov 04.34	−7.70	Lick-3 m/Kast	600	3500–8220	EG
2012 Nov 04.50	−7.54	ANU-2.3 m/WiFeS	900	3500–9550	MB, SK
2012 Nov 05.22	−6.82	NTT-3.6 m/EFOSC	100	3360–10000	PESSTO
2012 Nov 05.37	−6.67	Lick-3 m/Kast	600	3500–8220	EG
2012 Nov 05.61	−6.43	ANU-2.3 m/WiFeS	900	3500–9550	MB, SK
2012 Nov 06.38	−5.66	Lick-3 m/Kast	180	3500–10300	SBC, PK
2012 Nov 07.27	−4.77	NTT-3.6 m/EFOSC	100	3360–10000	PESSTO
2012 Nov 07.28	−4.76	du Pont/WFCCD	60	3500–9600	NM, BM
2012 Nov 07.34	−4.70	Lick-3 m/Kast	180	3500–8180	LP, DC
2012 Nov 08.24	−3.80	NTT-3.6 m/EFOSC	100	3360–10000	PESSTO
2012 Nov 08.27	−3.77	du Pont/WFCCD	60	3500–9600	NM, BM
2012 Nov 08.34	−3.70	Lick-3 m/Kast	180	3500–8180	LP, DC
2012 Nov 09.52	−2.52	ANU-2.3 m/WiFeS	900	3500–9550	FV
2012 Nov 09.62	−2.42	ANU-2.3 m/WiFeS	900	3500–9550	FV
2012 Nov 10.26	−1.78	du Pont/WFCCD	80	3500–9600	NM, BM
2012 Nov 10.57	−1.47	ANU-2.3 m/WiFeS	700	3500–9550	FV
2012 Nov 10.70	−1.34	ANU-2.3 m/WiFeS	900	3500–9550	FV
2012 Nov 11.26	−0.78	du Pont/WFCCD	90	3500–9600	NM, BM
2012 Nov 11.67	−0.37	ANU-2.3 m/WiFeS	900	3500–9550	FV
2012 Nov 12.38	+0.34	Lick-3 m/Kast	180	3500–8220	TD, JF
2012 Nov 12.74	+0.70	ANU-2.3 m/WiFeS	600	3500–9550	MO, MP
2012 Nov 13.24	+1.20	du Pont/WFCCD	270	3500–9600	JR, GB
2012 Nov 13.26	+1.22	NTT-3.6 m/EFOSC	100	3360–10000	PESSTO
2012 Nov 13.75	+1.71	ANU-2.3 m/WiFeS	600	3500–9550	MO, MP
2012 Nov 14.25	+2.21	du Pont/WFCCD	270	3500–9600	JR, GB
2012 Nov 14.32	+2.28	Lick-3 m/Kast	300	3500–10300	KC, OF
2012 Nov 15.22	+3.18	NTT-3.6 m/EFOSC	100	3360–10000	PESSTO
2012 Nov 15.24	+3.20	du Pont/WFCCD	270	3500–9600	JR, GB
2012 Nov 16.24	+4.20	du Pont / WFCCD	270	3500–9600	JR, GB
2012 Nov 16.51	+4.47	ANU-2.3 m / WiFeS	600	3500–9550	NS
2012 Nov 17.22	+5.18	du Pont / WFCCD	270	3500–9600	JR, GB
2012 Nov 17.46	+5.42	ANU-2.3 m / WiFeS	600	3500–9550	NS
2012 Nov 18.24	+6.20	du Pont / WFCCD	270	3500–9600	JR, GB
2012 Nov 18.42	+6.38	ANU-2.3 m / WiFeS	600	3500–9550	NS
2012 Nov 19.16	+7.12	du Pont / WFCCD	100	3500–9600	JR, GB
2012 Nov 19.56	+7.52	ANU-2.3 m / WiFeS	900	3500–9550	MC
2012 Nov 20.15	+8.11	du Pont / WFCCD	100	3500–9600	NM
2012 Nov 20.30	+8.26	Lick-3 m / Kast	360	3500–10300	SBC, OF
2012 Nov 20.48	+8.44	ANU-2.3 m / WiFeS	900	3500–9550	MC
2012 Nov 21.13	+9.09	du Pont / WFCCD	300	3500–9600	NM
2012 Nov 21.24	+9.20	NTT-3.6 m / EFOSC	100	3360–10000	PESSTO
2012 Nov 21.68	+9.64	ANU-2.3 m / WiFeS	900	3500–9550	MC
2012 Nov 23.25	+11.21	NTT-3.6 m / EFOSC	100	3360–10000	PESSTO
2012 Nov 29.42	+17.38	ANU-2.3 m / WiFeS	900	3500–9550	CL, BS
2012 Nov 30.08	+18.04	Baade / IMACS	900	3400–9600	DO
2012 Dec 04.21	+22.17	NTT-3.6 m / EFOSC	300	3360–10000	PESSTO
2012 Dec 08.50	+26.46	ANU-2.3 m / WiFeS	900	3500–9550	ITH
2012 Dec 12.22	+30.18	NTT-3.6 m / EFOSC	600	3360–10000	PESSTO
2012 Dec 16.92	+34.88	NOT / ALFOSC	300	3300–9100	MS
2012 Dec 17.41	+35.37	ANU-2.3 m / WiFeS	900	3500–9550	JM, CD, SO
2012 Dec 21.22	+39.18	NTT-3.6 m / EFOSC	900	3360–10000	PESSTO

Notes.
[a] With respect to *B*-band maximum brightness on 2012 November 12.04.
[b] BK, Beth Klein; BM, Barry Madore; BS, Brad Schaefer; BZ, Ben Zuckerman; CD, Catherine de Burgh-Day; CL, Chris Lidman; CM1, Curtis McCully; CM2, Carl Melis; DB, Daniel Bayliss; DC, Dan Carson; DO, David Osip; EG, Elinor Gates; FV, Frédéric Vogt; GB, Guillermo Blanc; GZ, George Zhou; ITH, I-Ting Ho; JF, Jerome Fang; JM, Jeremy Mould; JR, Jeff Rich; KC, Kelsey Clubb; LP, Liuyi Pei; MB, Mike Bessell; MC, Mike Childress; MJ, Michael Jura; MO, Matt Owers; MP, Mike Pracy; MS, Max Stritzinger; NM, Nidia Morrell; NS, Nic Scott; NSL, Nicola S. Loaring; OF, Ori Fox; PK, Pat Kellyl SBC, S. Bradley Cenko; SJ, Saurabh Jha; SK, Stefan Keller; SO, Sinem Ozbilgen; SX, Siyi Xu; TD, Tyler Desjardins.
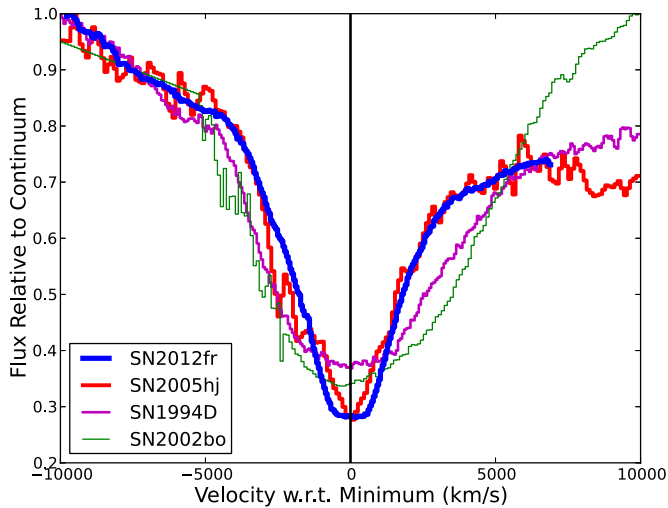[c] WiFeS red channel cryo pump failure.

Figure 2. Si II λ6355 feature of SN 2012fr (thick blue line) at +8 days in velocity space centered at the velocity minimum. Plotted for comparison are SN 2005hj (Quimby et al. 2007) at +9 days in red, SN 1994D (Blondin et al. 2012) at +11 days in magenta, and SN 2002bo (Benetti et al. 2004) at +5 days in green, in order of thickest to thinnest lines.

(A color version of this figure is available in the online journal.)

Table 2
Si II λ6355 Fit Results

Phase	HVF			Photospheric		
	v	Δv	pEW	v	Δv	pEW
(days)	(km s^{-1})	(km s^{-1})	(Å)	(km s^{-1})	(km s^{-1})	(Å)
−14.51	22704	11829	164.2	...	...	...
−14.17	22233	11587	171.6	...	...	...
−12.66	21525	9046	125.4	13444	6589	24.3
−12.53	21468	8898	120.2	13444	6294	23.0
−11.51	21223	7665	82.0	13430	6473	30.5
−10.05	20798	6315	43.5	13095	6547	38.0
−9.56	20374	6642	41.8	12685	6262	40.4
−9.35	20416	6326	37.6	12755	6431	43.0
−8.99	20275	6188	33.8	12595	6241	41.0
−8.47	20431	5767	29.5	12656	6347	46.8
−8.32	20327	5735	28.2	12571	6241	46.9
−7.97	20147	5503	22.6	12538	6041	46.2
−7.70	19902	6304	26.2	12057	6072	48.7
−7.54	20105	5735	24.5	12397	6167	51.3
−6.82	19501	5334	16.2	12284	5999	52.1
−6.67	19463	5545	16.2	11977	5978	53.6
−6.43	19817	4892	15.9	12251	6231	58.5
−5.66	19902	5651	16.1	12203	5841	55.5
−4.77	18713	5071	10.0	12104	5535	56.9
−4.70	18657	5345	9.8	11892	5619	58.3
−3.80	18397	5197	8.8	12048	5450	59.6
−3.70	18572	4892	5.5	11821	5398	58.4
−2.52	17242	4934	7.4	11944	5250	61.5
−2.42	18478	5693	8.0	12010	5377	63.9
−1.47	18006	4322	4.2	12057	5155	63.9
−0.37	...	...	...	12034	4965	63.4
+0.34	...	...	...	11821	4776	61.7
+0.70	...	...	...	12180	4755	62.9
+1.22	...	...	...	12175	4818	64.0
+1.71	...	...	...	12095	4617	62.8
+3.18	...	...	...	12156	4533	64.0
+4.47	...	...	...	12180	4270	62.3
+5.42	...	...	...	12109	4185	62.2
+6.38	...	...	...	12123	4132	62.4
+7.52	...	...	...	12227	3995	61.4
+8.44	...	...	...	12104	3953	61.1
+9.20	...	...	...	12118	3953	60.7
+9.64	...	...	...	12071	3953	61.3
+11.21	...	...	...	12006	...	...
+17.38	...	...	...	11732	...	...
+22.17	...	...	...	11423	...	...
+26.46	...	...	...	11794	...	...
+30.18	...	...	...	11829	...	...
+35.37	...	...	...	11771	...	...
+39.18	...	...	...	11716	...	...

a week after maximum brightness; (2) early-time spectra show clear signatures of a two-component Si II λ6355, indicating a layer of ejected material at higher velocities than the nominal photospheric layer; and (3) the velocity of the photospheric component remains constant (to within ∼200 km s^{-1}) until at least ∼40 days after maximum.

The clear detections of both the high-velocity (HV) layer and the constant photospheric velocity are facilitated by the extremely narrow velocity width of the photospheric absorption lines in SN 2012fr. In Figure 2, we show the Si II λ6355 width of SN 2012fr viewed in velocity space, compared to that of SN 2005hj (Quimby et al. 2007), SN 1994D (from Blondin et al. 2012), and SN 2002bo (Benetti et al. 2004). SN 2012fr has narrower Si II λ6355 than the other SNe Ia, except for perhaps SN 2005hj, whose similarly narrow line width was highlighted by Quimby et al. (2007). One can even visibly identify a flattening at the base of this feature due to the doublet nature of the line. We measure the observed line width (FWHM) to be ∼3400 km s^{-1}; if we account for the 14 Å separation of the doublet lines, then this implies an intrinsic line width of ∼3000 km s^{-1}.

3.1. High-velocity Si II λ6355 in Early-time Spectra

At two weeks before maximum light, Si II λ6355 appears to be composed of a single broad, HV component, but beginning around −12 days a second distinct component at lower velocities begins to develop. By −9 days the HVF and the lower velocity component exhibit equal strength, but by −5 days the HVF becomes difficult to distinguish visually.

While such Si II λ6355 HVFs have been observed in other SNe Ia, notably SN 2005cf (Wang et al. 2009b) and SN 2009ig (Foley et al. 2012; Marion et al. 2013; see also Section 6.1), the distinction between HVF and photospheric components is cleaner in SN 2012fr than ever seen before. In this section, we follow the evolution of the two components in a quantitative way by fitting the Si II λ6355 line as a simple double-Gaussian profile.

We show in Figure 3 some example fits of the Si II λ6355 line at several epochs. We first begin by defining regions of

the blue and red pseudo-continuum, then perform a simple linear fit between the two regions. The flux in the line region is next divided by the pseudo-continuum, and the normalized absorption profile is fitted with two Gaussians. The fit parameters are the center, width, and depth of each component, and the only constraints imposed are that the HVF component be above 14,000 km s^{-1} and the low-velocity photospheric component be below that same threshold. This threshold between the two fitted velocity components was chosen because it is higher than the velocities observed in most SNe Ia and provided favorable separation between the two velocity components.

In Table 2, we present the fitted parameters for our two-component Si II λ6355 fits including velocity center (v), velocity width (Δv; i.e., FWHM), and calculated pseudo-equivalent
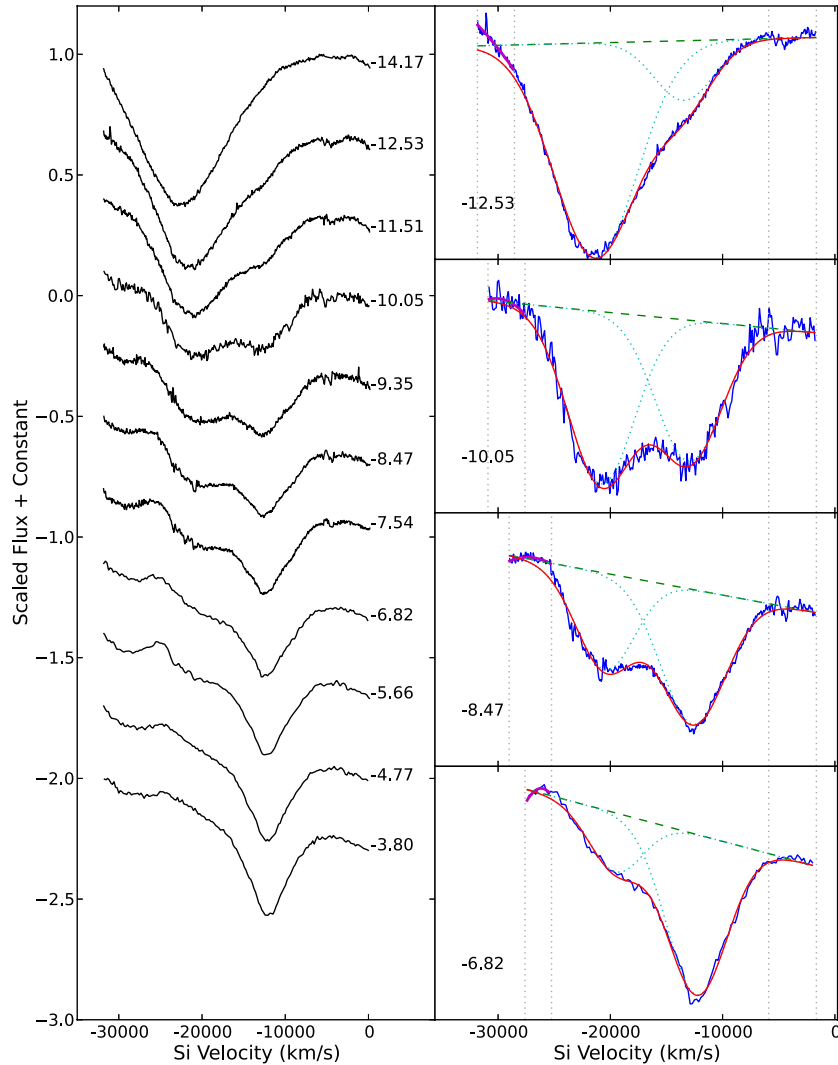
Figure 3. Left: evolution of the Si II λ6355 line of SN 2012fr in velocity space. Right: several representative examples of the two-component Gaussian fits. Data are in blue, regions of the pseudo-continuum fit are denoted by the vertical dotted black lines, the fitted pseudo-continuum is the dashed green line, the fully fitted profile is shown as the smooth red line, and the two individual components are the dotted cyan curves.

(A color version of this figure is available in the online journal.)

width (pEW). In Figure 4, we show the velocity evolution of the two components compared to the v_{Si} evolution of other SNe Ia from Benetti et al. (2005). The HVF component shows a strong velocity gradient ($\dot{v}_{Si} = 353$ km s^{-1} day^{-1}), but at velocities much higher than those seen in most SNe Ia, even at early times. The photospheric component, on the other hand, remains virtually constant in velocity even at late times (see Section 3.2), except for tentative evidence for higher velocity at the earliest epochs. However, we caution that the photospheric component is much weaker than the HVF component at those phases, so the velocity is more uncertain.

The relative strength of the two components is most clearly captured by examining the absorption strength of each component as quantified by the pEW. This can be trivially calculated as the area of the normalized absorption profile. We show in Figure 5 the pEW of the two fitted components from the earliest epoch (−13 days) to the latest epoch (−1 days) at which both features have a significant detection, and for the full Si II λ6355 profile for all epochs before +10 days. As previously noted, the strength of the HVF fades very quickly while that of the photospheric component slowly rises, with the equality point occurring between −10 and −9 days. The total pEW of the Si II λ6355

line declines until a few days before maximum light, when it remains nearly constant at around 65 Å. As we discuss below (Section 5), the pEW of this line is lower in SN 2012fr than in many other normal SNe Ia as measured in the Berkeley SN Ia Program (BSNIP) sample (Silverman et al. 2012a, 2012c).

3.2. Full Velocity Evolution of Si II λ6355

After the HVF Si II λ6355 feature fades, the main photospheric component is well fitted by a single Gaussian until about two weeks after maximum light. At that time, Fe lines to the red and blue of Si II λ6355 begin to develop significant opacity and make it impossible to correctly determine the pseudo-continuum of the Si II λ6355 line.

Thus, for the epochs +17 days and later, we fit the velocity minimum of Si II λ6355 by fitting a simple Gaussian profile only in a region of width 30 Å centered on the Si II λ6355 minimum. Remarkably, the velocity of the line minimum remains nearly constant at about 11,800 km s^{-1} even out to phase +39 days. This is confirmed by visual inspection of the Si II λ6355 region as plotted in Figure 6. We do note that at such late epochs, emission becomes increasingly important (see, e.g., van Rossum 2012)
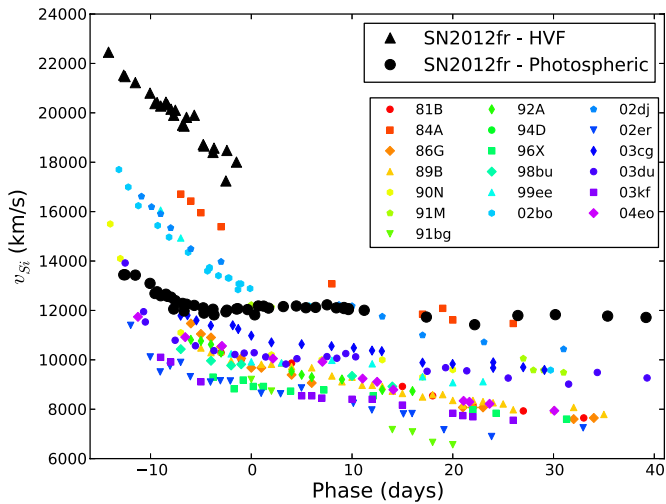
6

Figure 4. Velocity evolution of the Si II λ6355 feature of SN 2012fr compared to that of a number of SNe Ia from the Benetti et al. (2005) sample. The HVF component of SN 2012fr is shown as the large black triangles, while the lower velocity photospheric component is shown as large black circles.

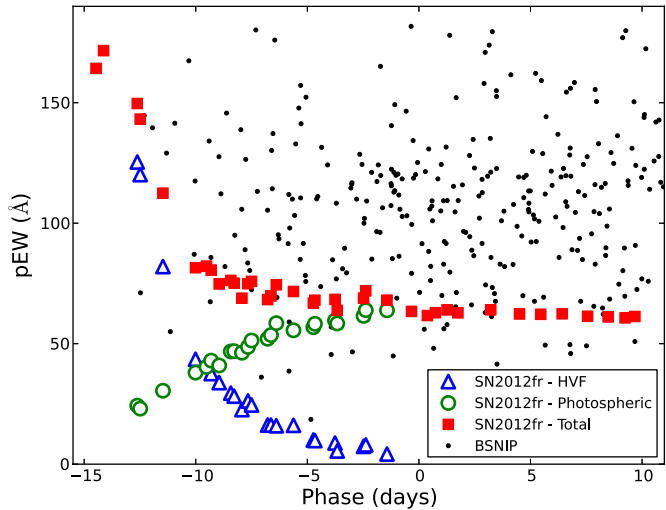(A color version of this figure is available in the online journal.)

Figure 5. Pseudo-equivalent width (pEW) of the Si II λ6355 components in SN 2012fr as a function of phase. When both the HVF and photospheric components are clearly detected, they are shown as open blue triangles and open green circles, respectively. The total pEW of the Si II λ6355 line is shown as filled red squares. For references, the BSNIP sample (Silverman et al. 2012a, 2012c) is shown as small black points.

(A color version of this figure is available in the online journal.)

Figure 6. Late-time evolution of the Si II λ6355 line in SN 2012fr, shown in velocity space. The wavelengths corresponding to 10,000 km s^{-1} and 15,000 km s^{-1} are shown as thick blue lines, with 1000 km s^{-1} intervals denoted by thin blue lines. The velocity plateau at late times appears around 11,800–12,000 km s^{-1}.

(A color version of this figure is available in the online journal.)

in the line profiles, so it is possible that the flux minimum may not necessary trace the true $\tau = 1$ surface.

We see once again that the narrow width of the photospheric lines provides an advantage in following the Si II λ6355 velocity reliably to very late epochs. The Fe lines to the red and blue of this feature are clearly distinguished in SN 2012fr, enabling an accurate isolation of Si II λ6355 and a reliable measurement of its velocity. In most other SNe Ia, the broader line widths result in a blend of the Si II λ6355 with its neighboring Fe lines, making velocity measurements difficult at late epochs. We will return to this point in Section 6.1.

4. ADDITIONAL ATOMIC SPECIES IN SN 2012fr

The narrow velocity width of the photospheric Si II λ6355 line noted in Section 3 holds true for nearly all absorption

features in the optical spectra of SN 2012fr starting about a week after maximum light. This provides a unique advantage in line identifications in the SN spectra, as blending of neighboring lines is less pronounced in SN 2012fr than in many other SNe Ia.

In this section, we focus on four element groups of particular interest. We begin by inspecting narrow Na I D absorption in Section 4.1 and show that SN 2012fr shows no detectable absorption in this line. We briefly present in Section 4.2 our search for signatures of unburned C, which showed no clear detection. In Section 4.3, we inspect the Ca II IR triplet, which exhibits behavior similar to that of Si II λ6355, and then briefly examine the more complex Ca II H&K line at maximum light. Finally, in Section 4.4, we examine the velocities of Fe-group elements in SN 2012fr.
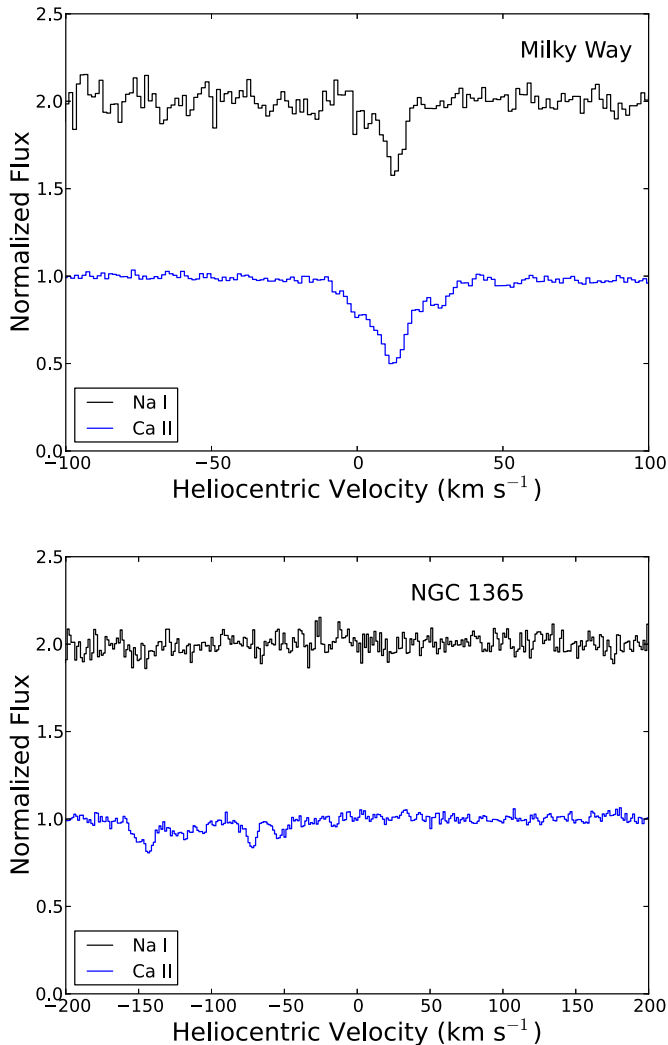
Figure 7. Keck HIRES observations of SN 2012fr. Top: narrow Na I D and Ca II H&K at rest velocity, arising from the Milky Way gas. Bottom: narrow Na I D and Ca II H&K at the recession velocity of NGC 1365.

(A color version of this figure is available in the online journal.)

Table 3
HIRES Absorption Equivalent Widths

Line	Milky Way (mÅ)	NGC 1365 (mÅ)
Ca II λ3934.777	129.3 ± 3.6	107.3 ± 7.0
Ca II λ3969.591	66.0 ± 4.0	57.3 ± 6.0
Na I λ5891.5833	82.9 ± 13.8	<42.0 (3σ)
Na I λ5897.5581	35.4 ± 13.4	<40.8 (3σ)

to convert Na I D absorption into the reddening $E(B-V)$, the measured D1 and D2 absorption strengths imply reddenings of $E(B-V) = 0.0186$ and $E(B-V) = 0.0213$ mag, respectively. These are in excellent agreement with the measured value of $E(B-V) = 0.018$ mag from Schlafly & Finkbeiner (2011).

The only possible absorption features at the redshift of NGC 1365 appear in the Ca II H&K lines at $v \approx -100$ km s^{-1} from the rest redshift of NGC 1365. Given that these features lack corresponding ones in Na I D, in addition to the facts that NGC 1365 is a nearly face-on barred spiral and SN 2012fr is very close to the center of the galaxy and thus well away from the dusty spiral arms, it appears unlikely that this feature near Ca II H&K is truly caused by interstellar gas. Thus, we detect no significant narrow absorption features in SN 2012fr. Given the traditional correlation of these narrow absorption features with reddening by foreground dust, our observations are consistent with SN 2012fr having no obscuration by foreground dust. The strongest constraint arises from the D2 line of Na I, which places a 3σ upper limit of $E(B-V) < 0.015$ mag (again using Poznanski et al. 2012) for the reddening of SN 2012fr from within NGC 1365.

4.2. C II

We comment briefly in this section on the search for unburned C features in spectra of SN 2012fr. Such signatures typically manifest themselves as weak C II absorption lines in optical spectra of SNe Ia and have been of particular interest in recent years (Thomas et al. 2011a; Parrent et al. 2011; Folatelli et al. 2012; Silverman & Filippenko 2012; Blondin et al. 2012). The strongest C feature in the optical is typically the C II λ6580 line, and the slightly weaker λ7234, λ4745, and λ4267 lines of C II are also sometimes visible (e.g., Mazzali 2001; Thomas et al. 2007).

The redshift of NGC 1365 places the likely location of the blueshifted absorption minimum of C II λ6580 coincident with a weak telluric absorption feature at $\lambda = 6280$ Å (corresponding to $v \approx 13,700$ km s^{-1} for C II λ6580). This telluric line is of comparable strength to the typical C II absorption, but it was entirely or largely removed during the reduction process. We cannot identify any obvious signature of C II λ6580 absorption at its position; nor do we detect the other major optical C II lines even at early epochs.

This is demonstrated directly in Figure 8, where we plot regions around the four C II lines in velocity space for the -14.17 day spectrum from SALT. No clear signature of C II seems visible in any of these lines, even for C II λ6580 after removal of the telluric feature. C I features in the NIR may provide better detection of unburned material in SN 2012fr (see, e.g., SN 2011fe in Hsiao et al. 2013) and will be investigated with detailed spectroscopic fitting in Paper III (E. Y. Hsiao et al. 2013, in preparation).
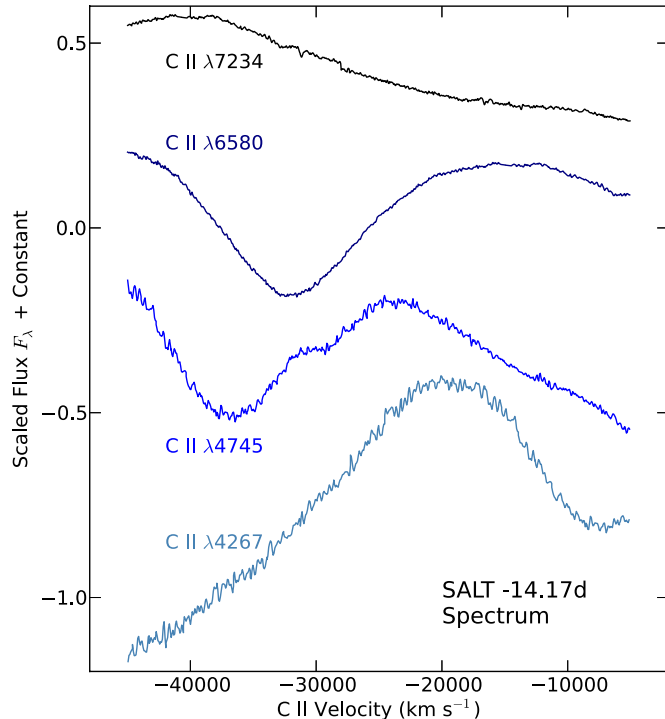
4.1. Na I D Narrow Absorption

Narrow absorption in the Na I D line in SN Ia spectra is commonly used to quantify the amount of foreground dust that reddens an SN Ia (dust is associated with the detected gas). Na I D absorption at the redshift of the SN host galaxy presumably arises from either foreground interstellar gas (e.g., Poznanski et al. 2011, 2012) or very nearby circumstellar material (CSM) shed from the SN progenitor system prior to explosion (Patat et al. 2007; Simon et al. 2009; Sternberg et al. 2011; Dilday et al. 2012).

SN 2012fr shows no detectable narrow Na I D absorption in the HIRES spectrum taken at phase -13.6 days. In Figure 7, we show the regions of the HIRES spectrum corresponding to the Na I D line as well as the Ca II H&K lines, both at the redshift of the host galaxy NGC 1365 ($v = 1636$ km s^{-1}; Bureau et al. 1996) and at zero redshift. Measurements of the line detections, or 3σ upper limits, are presented in Table 3.

Narrow absorption features from the Milky Way gas are clearly detected at 2.6σ and 6.0σ in the D1 and D2 lines of Na I, and at very high significance ($>10\sigma$) in the H&K lines of Ca II. Using the empirical scaling relations of Poznanski et al. (2012)

Figure 8. Sections of the -14.17 day SALT spectrum of SN 2012fr corresponding to the strongest typical C II features in SNe Ia, plotted in terms of velocity of the respective lines.

(A color version of this figure is available in the online journal.)

4.3. Ca II

4.3.1. Ca II Infrared Triplet

The Ca II IR triplet in SN 2012fr begins at very high velocities two weeks before maximum light, with the blue edge of the absorption in the first spectrum reaching relativistic velocities of nearly 50,000 km s^{-1} ($v \approx 0.17c$). The line complex gradually recedes in velocity and exhibits complex structure roughly a week before maximum light, and by two weeks after maximum it appears dominated by a single narrow component.

The complex structure of the Ca II IR triplet appears to be indicative of multiple components in velocity space, similar to that seen in the Si II $\lambda6355$ line (see Section 3.1). Modeling this line multiplet is more complex than the simple two-component Gaussian fits employed for Si II $\lambda6355$. Instead, each component of the Ca II IR triplet in velocity space must be modeled as a triplet of Gaussian profiles with common velocity width, separation in velocity space as dictated by the line rest wavelengths, and with relative absorption depths appropriately constrained.

For epochs where spectral coverage extended to sufficiently red wavelengths to cover the Ca II IR triplet, we fit the absorption profile as a two-component model after normalizing to a fitted pseudo-continuum. Each absorption component is described by a central velocity, velocity width, and absorption depth (here we set relative absorption depths of the triplet lines to be equal, assuming the optically thick regime). As with Si II $\lambda6355$, the only constraint applied here was to force the two components to occupy different regions of velocity space split at 14,000 km s^{-1}. We show the spectral evolution of the Ca II IR triplet as well as some representative profile fits in Figure 9. As with the Si II $\lambda6355$ fits, the pseudo-continuum shape begins to be poorly represented by a simple linear fit at late times. Thus, we employ

Table 4
Ca II IR Triplet Fit Results

Phase	HVF			Photospheric		
	v	Δv	pEW	v	Δv	pEW
(days)	(km s^{-1})	(km s^{-1})	(Å)	(km s^{-1})	(km s^{-1})	(Å)
-14.51	31087	21853	615.5	. . .	. . .	. . .
-11.51	28640	15311	364.8	. . .	. . .	. . .
-9.35	25571	9581	146.9	. . .	. . .	. . .
-7.54	24126	5507	94.5	11221	1629	4.1
-4.77	23043	5808	99.7	11259	2407	13.2
-2.52	21994	6226	96.1	11219	2697	29.9
-0.37	20989	6662	90.0	11357	3151	49.5
$+1.22$	20131	6935	82.9	11461	3187	60.3
$+3.18$	19133	7368	78.2	11564	3207	70.8
$+5.42$	15913	10582	121.5	11690	2769	52.9
$+8.44$	. . .	. . .	. . .	12206	. . .	. . .
$+11.21$	. . .	. . .	. . .	12240	. . .	. . .
$+17.38$	. . .	. . .	. . .	12092	. . .	. . .
$+22.17$	. . .	. . .	. . .	12121	. . .	. . .
$+26.46$	. . .	. . .	. . .	11976	. . .	. . .
$+30.18$	. . .	. . .	. . .	12082	. . .	. . .
$+35.37$	. . .	. . .	. . .	11937	. . .	. . .
$+39.18$	. . .	. . .	. . .	12052	. . .	. . .

a similar Gaussian line minimum fitting technique as that for Si II $\lambda6355$ at epochs after $+8$ days, here measuring the minimum of the cleanly separated 8662 Å line.

We report results in Table 4, with fit parameters labeled similarly as in Table 2. The HV component consistently exhibits a broad velocity width (>5000 km s^{-1}), producing a broad component where all lines in the triplet are blended. The low-velocity component exhibits the same narrow velocity width as observed in the Si II $\lambda6355$ line, making it possible to distinguish the 8662 Å line from the blended 8498 Å and 8542 Å lines. This is illustrated directly in Figure 10, where we show the Ca II IR triplet evolution at late times and demonstrate the ability to both resolve the triplet lines and observe their consistent velocity at $v \approx 12,000$ km s^{-1}.

In Figure 11, we plot the velocity evolution of the fitted Ca II IR triplet components compared to the analogous components in the Si II $\lambda6355$ line (Section 3). The HVF Ca II IR triplet component is consistently at higher velocities than the Si II $\lambda6355$ HVF, has a steeper velocity gradient ($\dot{v}_{Ca} = 686$ km s^{-1} day^{-1}), and is visible to later epochs than the Si II $\lambda6355$ HVF (we note that these characteristics were also observed in the Ca II IR triplet feature of SN 2009ig; Marion et al. 2013). In SN 2012fr, the late-time velocity of the Ca II IR triplet plateaus at $v \approx 12,000$ km s^{-1}, consistent with the velocity plateau observed in the Si II $\lambda6355$ line.

Finally, we comment on the dependence of our results on the assumption of optical thickness in the Ca II IR triplet. We repeated the above fits under the assumption of the optically thin regime, where the relative absorption depths of the triplet lines are proportional to their Einstein B (absorption) values (1.71×10^9 cm^2 s^{-1} erg^{-1} for $\lambda8498$, 1.03×10^{10} cm^2 s^{-1} erg^{-1} for $\lambda8542$, and 8.66×10^9 cm^2 s^{-1} erg^{-1} for $\lambda8662$; Wiese et al. 1969) and the relevant statistical weights, and found that the qualitative behavior of the velocity evolution was consistent with that found in our fiducial fits. The velocities of the HVF Ca II IR triplet component were consistently higher due to the shift in weighted mean wavelength of the triplet, but the late-time velocity was still consistent with the $v \approx 12,000$ km s^{-1} velocity plateau due to the 8662 Å line being
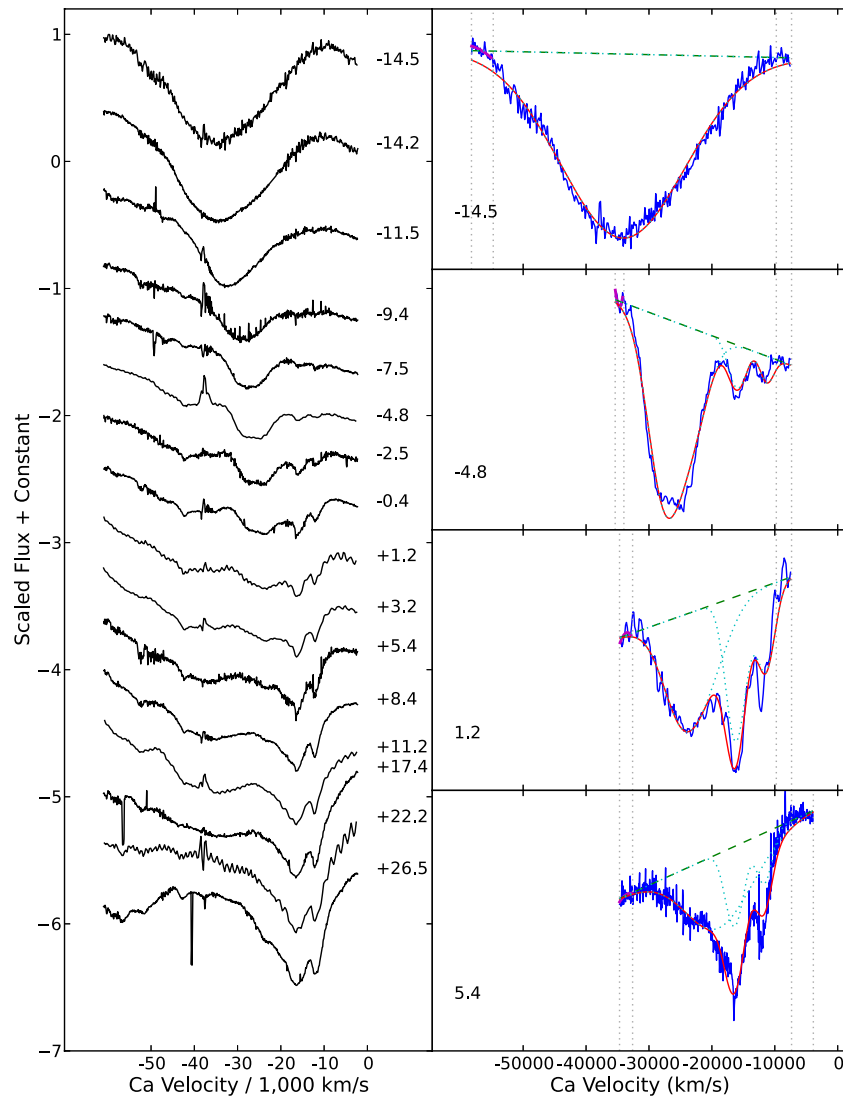
Figure 9. Same as Figure 3, but for the Ca II IR triplet. Here velocities are plotted with respect to the reddest line in the Ca II IR triplet at 8662 Å.
(A color version of this figure is available in the online journal.)

distinguishable from the bluer lines in the triplet. Interestingly, the photospheric component appears to be better fitted (and yields a velocity consistent with the velocity plateau) in the optically thin assumption at early epochs, and then transitions to being optically thick around the time when the HVF component fades. The true absorption strengths of the lines in the Ca II IR triplet likely fall somewhere between the optically thin and optically thick regimes, but we have confirmed that our results are consistent in both extreme cases.

4.3.2. Ca II H&K

The Ca II H&K doublet in SNe Ia is a line complex of keen interest, as its behavior at maximum light may be an indicator of intrinsic SN Ia color (Foley et al. 2011; Chotard et al. 2011; Blondin et al. 2012; Foley 2012). Additionally, recent work by Maguire et al. (2012) showed that the Ca II H&K velocity of the mean rapidly declining (low "stretch") SN Ia spectrum at maximum light is lower than that of the mean slowly declining (high "stretch") SN Ia spectrum. Thus, the Ca II H&K line seems promising for helping to unravel SN Ia diversity.

Interpreting Ca II velocities with this line complex is difficult, however, due to the presence of the nearby Si II λ3858 line

(see the thorough discussion in Foley 2012), as well as the complex underlying pseudo-continuum. We therefore chose to examine this line complex only at maximum light for SN 2012fr. We employed a fitting procedure similar to that of the Ca II IR triplet, but with fit parameters informed and tightly constrained by the results of the Ca II IR triplet and Si II λ6355 fits. We model absorption in the Ca II H&K line with multiple velocity components, where each component is a doublet profile with relative depths set to unity (i.e., the optically thick regime). In addition to the HVF and photospheric components of the Ca II H&K line, we add a single Gaussian absorption profile to model Si II λ3858. We note that fits assuming the optically thin regime (with line depths proportional to the Einstein B values of $4.50 \times 10^{10} \, \mathrm{cm^2 \, s^{-1} \, erg^{-1}}$ for λ3934 and $2.20 \times 10^{10} \, \mathrm{cm^2 \, s^{-1} \, erg^{-1}}$ for λ3968; Wiese et al. 1969) produced poor fits to the Ca II H&K line, especially the photospheric component.

To enforce consistency with the other lines measured for Ca and Si, we constrained the velocity center and velocity widths of the two Ca II H&K components to be within 20% of their values fitted for the Ca II IR triplet, but left the absorption depths as free parameters. Similarly, we forced the velocity width and
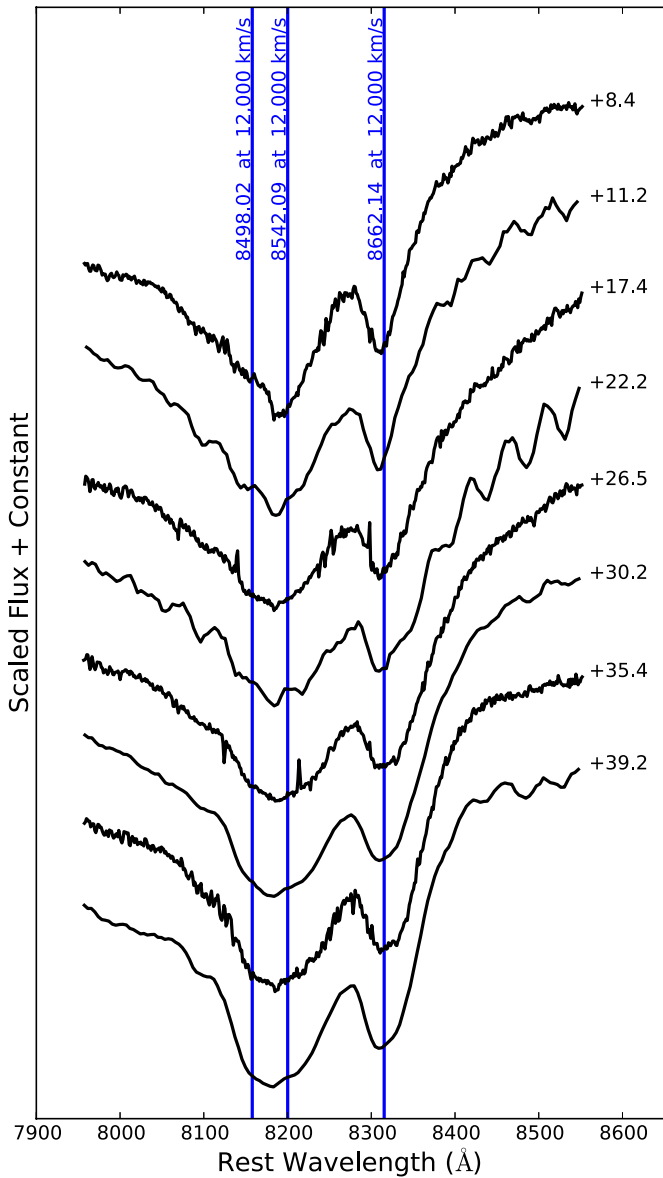
Figure 10. Late-epoch evolution of the Ca II IR triplet in SN 2012fr, showing the narrow velocity width and constant velocity of the three lines comprising the triplet. For reference, we mark the wavelengths of the three triplet lines at a velocity of $v = 12{,}000$ km s^{-1}, showing that the reddest line of the triplet at 8662 Å is cleanly resolved from the bluer two lines.

(A color version of this figure is available in the online journal.)

Figure 11. Velocity evolution of the high-velocity (triangles) and photospheric (circles) components of the Ca II IR triplet (open red symbols) in SN 2012fr compared to that of the Si II λ6355 line (filled blue symbols).

(A color version of this figure is available in the online journal.)
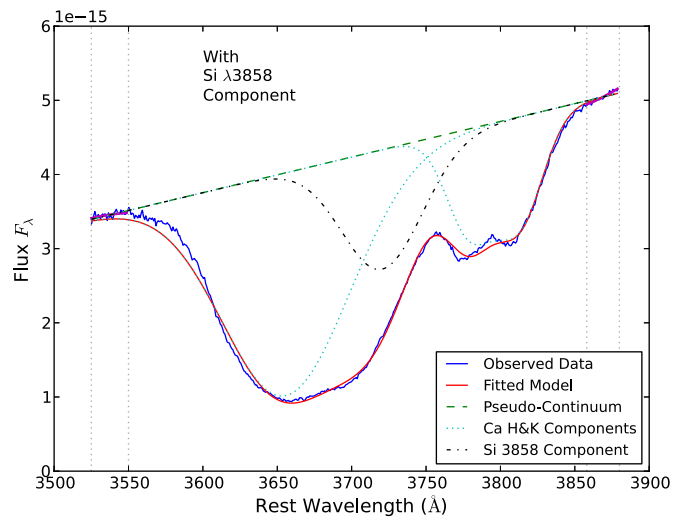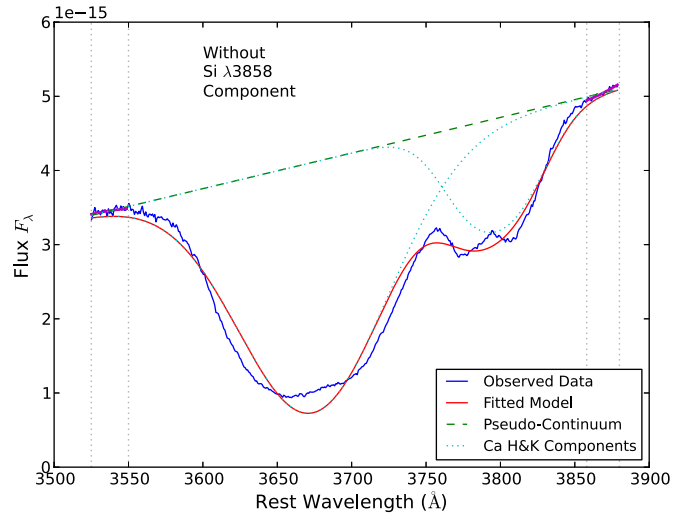
Figure 12. Fit to the Ca II H&K line profile in the maximum-light (WiFeS November 11.67) spectrum of SN 2012fr. The line colors and styles are the same as in Figure 3, but with the Si II λ3858 line profile plotted as the dash-dotted black line. The top panel shows a fit without the Si II λ3858 line, while the bottom panel shows a fit including this line.

(A color version of this figure is available in the online journal.)

center of the Si II λ3858 line to be within 20% of the Si II λ6355 line. To investigate the importance of the Si II λ3858 line in this complex, we performed fits both with and without the Si II λ3858 line included, and our best fits for each case are shown in Figure 12.

In Table 5, we summarize the main results of our Ca II H&K line fits, for the cases with and without Si II λ3858, as well as the Ca II IR triplet and Si II λ6355 results for reference. Both Ca II H&K fits yield Ca and Si velocities within 1000 km s^{-1} of their red counterparts, but the fit with Si II λ3858 included shows a more favorable ratio of pEW for the photospheric and HVF Ca components, as well as a much better fit to the overall line profile. Our fits indicate that both Ca II H&K and Si II λ3858 are needed to explain the absorption profile of the Ca II H&K line complex in SN 2012fr, with the HV Ca II H&K being dominant over the Si II λ3858.

Table 5
Ca II H&K Fit Results

	Ca HVF			Ca Photospheric			Si Photospheric		
	v (km s^{-1})	Δv (km s^{-1})	pEW (Å)	v (km s^{-1})	Δv (km s^{-1})	pEW (Å)	v (km s^{-1})	Δv (km s^{-1})	pEW (Å)
Ca NIR + Si II λ6355	20989	6662	96.1	11357	3151	49.5	12034	4965	. . .
Ca H&K + Si II λ3858	22545	6633	79.9	11775	2675	23.6	10749	4707	25.4
Ca H&K only	21216	7994	103.3	11787	3665	23.8	. . .	. . .	. . .

We note, however, that the quantitative details of these results depend on how tightly we constrain the velocity center and width of the HV Ca II H&K component. If we loosened the constraints to be within 30% of the Ca II IR triplet velocity and width, then it changes the pEW of the HV Ca II H&K and Si II λ3858 lines to be 68 Å and 35 Å, respectively, from 80 Å and 24 Å when constrained to 20%. This is because the high velocities of the HV Ca II H&K component place it nearly coincident with the wavelength of the lower velocity Si II λ3858 line. We therefore cannot say conclusively what the absorption ratio of these two lines is in this line complex, but we did find consistently that both were needed to adequately fit the absorption profile.

We found here that decoupling the Si II λ3858 line from the Ca II H&K line is a nontrivial procedure. While it is difficult to derive precise quantitative results, two general qualitative results are clear. The first is that both the Ca II H&K line and the Si II λ3858 line are operative in this line complex in SN 2012fr, and that HV Ca II H&K can be nearly degenerate with lower velocity Si II λ3858. The second conclusion for SN 2012fr is that regardless of the details of how much the line velocities and velocity widths are allowed to vary, HV Ca II H&K appears to be the dominant contributor to absorption in this line region.

4.4. Fe-group Elements

The relatively narrow line widths of SN 2012fr are useful for identifying absorption features, which are typically blended in other SNe Ia, and are particularly advantageous for identifying Fe lines. In Figure 13, we illustrate this principle with the +8 day spectrum of SN 2012fr compared to two other "normal" SNe Ia, SN 2005cf (Wang et al. 2009b) and SN 2003du (Stanishev et al. 2007), as well as to the broad-lined SN 2002bo (Benetti et al. 2004). Of particular note is the line complex at ~4700 Å, comprising several Fe II lines and the Si II λ5054 line, which shows cleaner separation in SN 2012fr than the other SNe Ia.

In the +8 day spectrum, three major Fe II lines (λ4924, λ5018, and λ5169) all have velocity minima consistent with the velocity plateau ($v \approx 12{,}000$ km s^{-1}) identified in Si II λ6355. We illustrate this in Figure 14, where we plot the post-maximum spectra of SN 2012fr in the relevant wavelength region and highlight the wavelengths associated with each of these lines at $v = 12{,}000$ km s^{-1}. After this epoch, the observed velocity minima of these Fe lines decrease with time. We also tentatively identify two features that may be associated with Cr II lines (λ4876 and λ5310), though their velocity evolution is more difficult to follow due to the strongly evolving shape of the underlying pseudo-continuum. We note here that these lines which we attribute to Fe-group elements show no clear signature of HVFs in the early-time spectra of SN 2012fr (some Fe HVFs have been possibly identified in several SNe Ia; e.g., Branch et al. 2004; Mazzali et al. 2005b; Marion et al. 2013), though further modeling of the spectra may reveal more subtle insights.

The velocity behavior of the Fe-group lines indicates that the $\tau = 1$ surface of the photosphere is at $v \approx 12{,}000$ km s^{-1} one
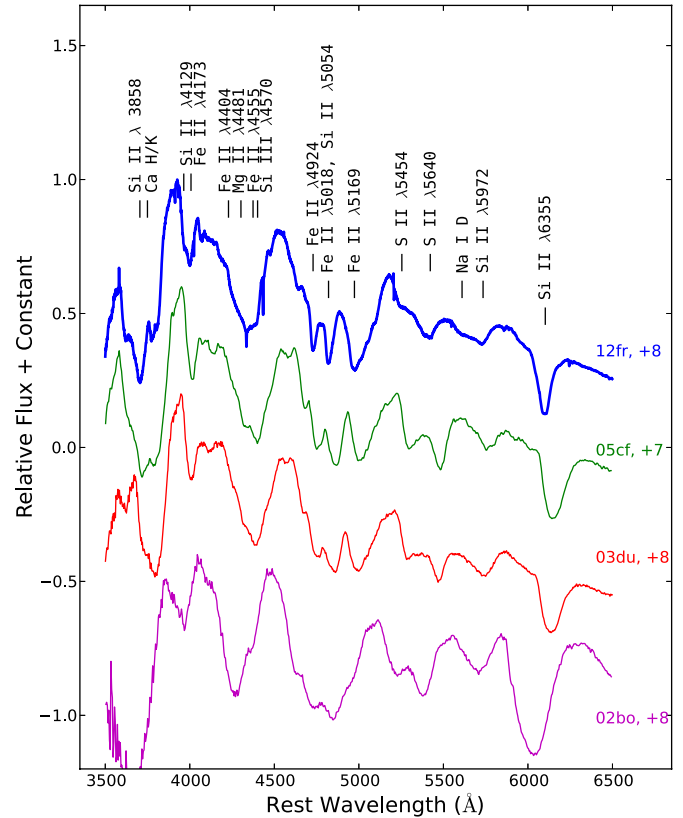

Figure 13. Line identifications in SN 2012fr (blue) for the +8 day spectrum, compared to the spectra of other SNe Ia at a similar epoch. SN 2005cf (Wang et al. 2009b), SN 2003du (Stanishev et al. 2007), and SN 2002bo (Benetti et al. 2004) are shown as the green, red, and magenta spectra, respectively.

(A color version of this figure is available in the online journal.)

week after maximum brightness, and recedes inward after that time. From this we can conclude two important results: (1) the Si and Ca velocity plateaus imply that the layer of intermediate-mass elements (IMEs) is unlikely to extend deeper than $v \approx 12{,}000$ km s^{-1} since the Fe-group elements are detected at lower velocities at the same epochs; and (2) the layer of Fe-group elements extends deeper in the ejecta than the IMEs, indicating a likely stratification of the ejecta.

While these preliminary line identifications are interesting, a full accounting of all elements and their velocities would require a spectrum-synthesis fit (see, e.g., Thomas et al. 2011b) such as that undertaken by Parrent et al. (2012) for SN 2011fe (Nugent et al. 2011; Li et al. 2011), or a modeling of abundance stratification in the ejecta such as that undertaken by Stehle et al. (2005). Analyses of this magnitude are beyond the intended scope of this paper, but we believe that the spectra released here will be invaluable for such efforts, and we strongly encourage future modeling of the SN 2012fr spectra.
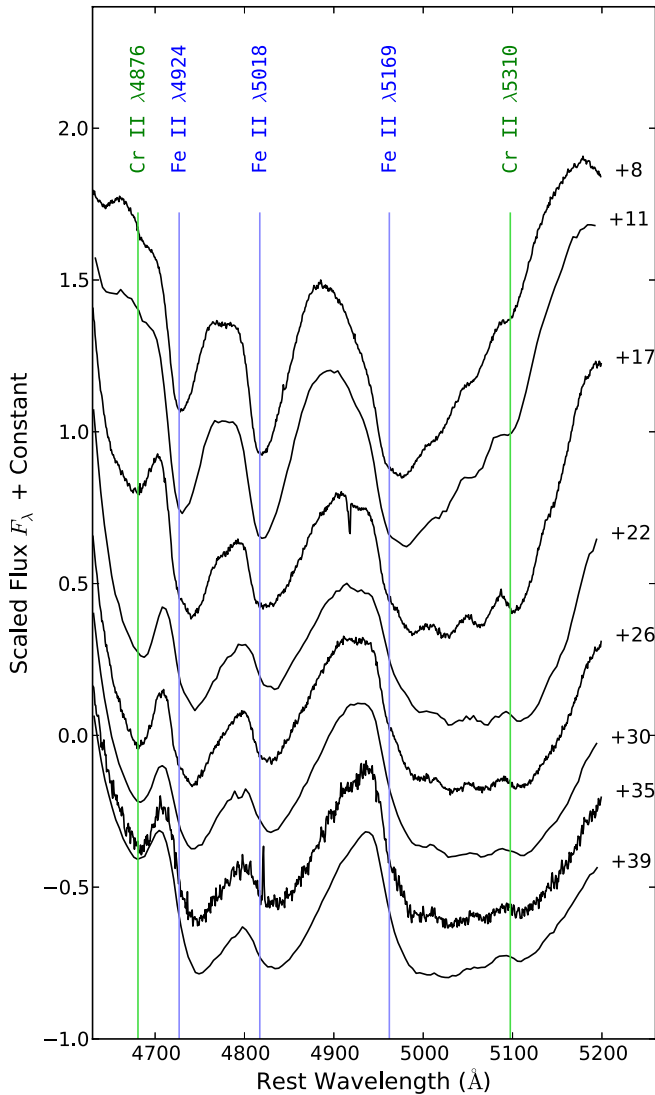
Figure 14. Post-maximum spectra of SN 2012fr highlighting a selected region having significant features of Fe-group elements. The vertical lines correspond to wavelengths of labeled features at $v = 12{,}000$ km s^{-1}, the measured velocity of Fe II features in the +8 day spectrum.

(A color version of this figure is available in the online journal.)

Table 6
Spectral Indicators for SN 2012fr

Quantity	Value	Unit
$\Delta m_{15}(B)$	0.80 ± 0.01	mag
pEW(5972)	3.9 ± 5.0	Å
pEW(6355)	66.5 ± 15.5	Å
v_{Si} (max)	12037 ± 200	km s^{-1}
$\dot{v}_{Si}$	0.3 ± 10.0	km s^{-1} day^{-1}

5. SPECTROSCOPIC SUBCLASSIFICATION OF SN 2012fr

In recent years, much effort has been focused on categorizing the observed diversity of SNe Ia by means of quantitative metrics measured from their optical spectra. In this section, we will examine SN 2012fr in the context of these classification schemes. The spectral indicator values of SN 2012fr employed for that purpose are presented in Table 6. These include several quantities (pEW(5972), pEW(6355), v_{Si})

calculated from the maximum-light spectrum (the November 11.67 WiFeS spectrum), the velocity gradient of the Si II λ6355 line $\dot{v}_{Si}$ (measured from the absolute decline between phases 0 and +10 days), and the light-curve decline $\Delta m_{15}(B)$ (from Paper II). We note that the pEW values used here are calculated from direct integration of the line profile and differ insignificantly from the Gaussian area reported in Section 3.1.

Branch et al. (2009) proposed that SNe Ia can be split into four broad categories based on their location in the parameter space defined by the pEW of the Si II λ5972 and λ6355 lines. We show SN 2012fr on this "Branch diagram" in the upper-left panel of Figure 15, along with a set of SNe Ia combining the samples of Blondin et al. (2012) and Silverman et al. (2012c). SN 2012fr falls on the boundary between the "shallow silicon" class and the "core normal" class. As previously noted by both Silverman et al. (2012c) and Blondin et al. (2012), these Branch classes do not represent disjoint samples with distinct features, but instead regions within a continuum of SN Ia characteristics. SN 2012fr appears to be a clear example of a transition-like event that bridges the gap between two subclasses.

Wang et al. (2009a) showed that a subset of SNe Ia display high velocities in the Si II λ6355 line, and this "HV" subset exhibits different color behavior than SNe Ia with normal velocities. In the upper-right panel of Figure 15, we show SN 2012fr on the "Wang diagram" which plots pEW(6355) versus v_{Si} at maximum light, as well as the same comparison sample of SNe Ia from the Branch diagram. Once again, SN 2012fr has a v_{Si} value that is just slightly above the established boundary separating HV from normal SNe Ia, marking it as a transition-like event between velocity classes. Its location in this diagram is noteworthy because it exhibits a lower pEW(6355) than any of the other HV SNe Ia, and its velocity is higher than that of other SNe Ia having weak Si II λ6355 absorption.

Benetti et al. (2005) examined subclasses of SNe Ia based on the velocity evolution of the Si II λ6355 line. They found that rapidly declining SNe Ia tended to have consistently high velocity gradients (dubbed the "faint" subclass), while slowly declining SNe Ia appeared to occur in two classes with either high or low velocity gradients ("HVG" and "LVG," respectively). In the bottom-left panel of Figure 15, we show SN 2012fr on this "Benetti diagram" along with the subset of SNe Ia from the other panels with sufficient data to measure a velocity gradient. SN 2012fr clearly resides in the LVG region of this diagram, as expected due to the observed Si II λ6355 velocity plateau (see Section 3.2).

Finally, in the bottom-right panel of Figure 15, we show the velocity gradient versus velocity at maximum light. As has been previously noted, the HV objects appear to show a correlation between their velocity gradient and velocity at maximum light. SN 2012fr has a lower velocity gradient than any of the HV members, and instead appears to reside at the edge of the cloud of points populated by normal-velocity SNe Ia.

SN 2012fr exhibits much of the spectroscopic and photometric behavior of the more luminous SNe Ia such as SN 1991T (Phillips et al. 1992; Filippenko et al. 1992) or SN 1999aa (Li et al. 2001; Garavini et al. 2004). It has a slow light-curve decline rate, relatively shallow Si II absorption at maximum light, and a very low velocity gradient in the Si II λ6355 line. However, two key features of SN 2012fr are not observed in SN 1999aa-like or SN 1991T-like SNe Ia: the HV of the Si II λ6355 line (both at maximum light in the photospheric component and in the early HVF component) and strong absorption in the Si II λ6355 line at early epochs (phase about -10 days).
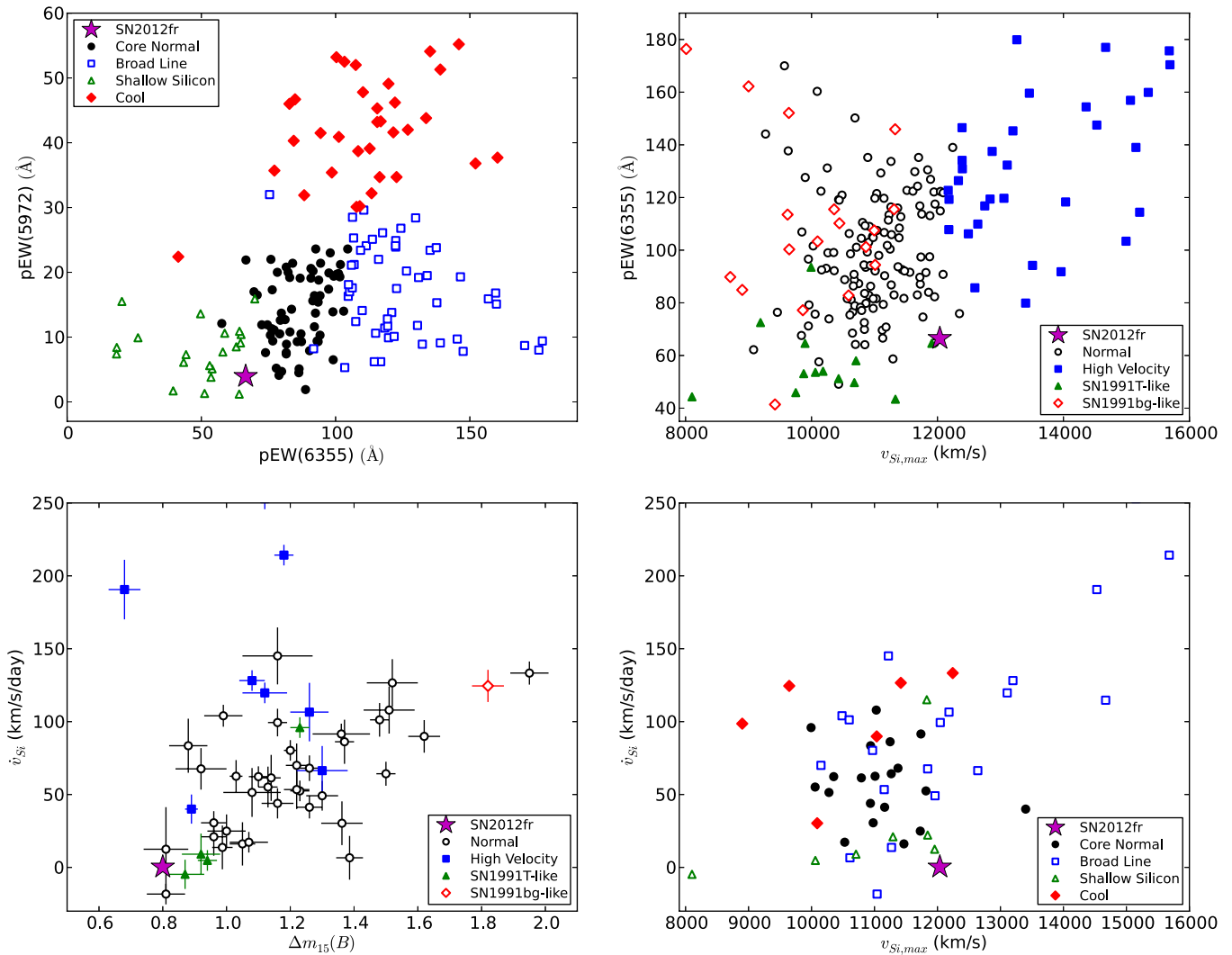
Figure 15. Spectral indicators from SN 2012fr compared to those of other SNe Ia as measured by Blondin et al. (2012) and Silverman et al. (2012c). Top left: pEW(5972) vs. pEW(6355) at maximum light with spectroscopic subclasses as defined by Branch et al. (2009). Top right: pEW(6355) vs. v_{Si} at maximum light with velocity-based subclasses as defined by Wang et al. (2009a). Bottom left: velocity gradient of the Si II λ6355 line $\dot{v}_{Si}$, as measured from the absolute decline between phases 0 and +10 days, vs. light-curve decline $\Delta m_{15}(B)$, as previously inspected by Benetti et al. (2005). Bottom right: velocity gradient vs. v_{Si} at maximum light.

(A color version of this figure is available in the online journal.)

In Figure 16, we compare the spectra of SN 2012fr at −12 days and at maximum light to comparable spectra from the SN 1991T-like SN 1998es (from Blondin et al. 2012), SN 1999aa (from Blondin et al. 2012), and the normal SNe Ia SN 2005cf (Wang et al. 2009b) and SN 2003du (Stanishev et al. 2007). We see that at maximum light, SN 2012fr shows slightly weaker Si II λ5972 and Si II λ6355 than the normal SNe Ia, but higher velocity and stronger Ca H&K absorption than SN 1999aa and the SN 1991T-like SN. At very early epochs (−12 days), SN 2012fr is very dissimilar to the extremely slow decliners, as it displays stronger absorption in Si II λ6355 and the "sulfur W," and it lacks the characteristic strong Fe absorption found in SN 1999aa/SN 1991T-like SNe Ia. The stronger absorption and higher velocities of the photospheric components of the Si II λ6355 line and the lack of strong Fe absorption also argue against the possibility of SN 2012fr being an SN 1999aa/SN 1991T-like SN Ia with HVFs superposed on its spectrum. Thus, while SN 2012fr shares a number of characteristics with these very slowly declining SNe Ia, it does not exhibit sufficient spectroscopic similar to be classified as a member of this peculiar SN Ia subclass.

6. DISCUSSION

The spectra of SN 2012fr exhibit several noteworthy characteristics: (1) a very narrow velocity width in the photospheric absorption lines for phases later than one week after maximum light; (2) HVFs Si II λ6355 and Ca II IR triplets which could be cleanly decoupled from the lower velocity photospheric component; (3) a clear plateau in the Si II λ6355 and the Ca II IR triplet velocities, extending out until +39 days; (4) Si absorption-line strengths placing it on the borderline between "shallow silicon" and "core normal" classes; and (5) Si velocity placing it on the borderline between "normal" and "HV" SNe Ia.

In this section, we first reflect on what the Si II λ6355 velocity behavior of SN 2012fr can reveal about interpretation of this velocity evolution in other SNe Ia (Section 6.1). We then consider how the aforementioned observational characteristics of SN 2012fr inform us about the probable nature of its explosion (Section 6.2). Finally, we consider the viability of SN 2012fr as a fundamental calibrator for measuring the Hubble constant (Section 6.3).
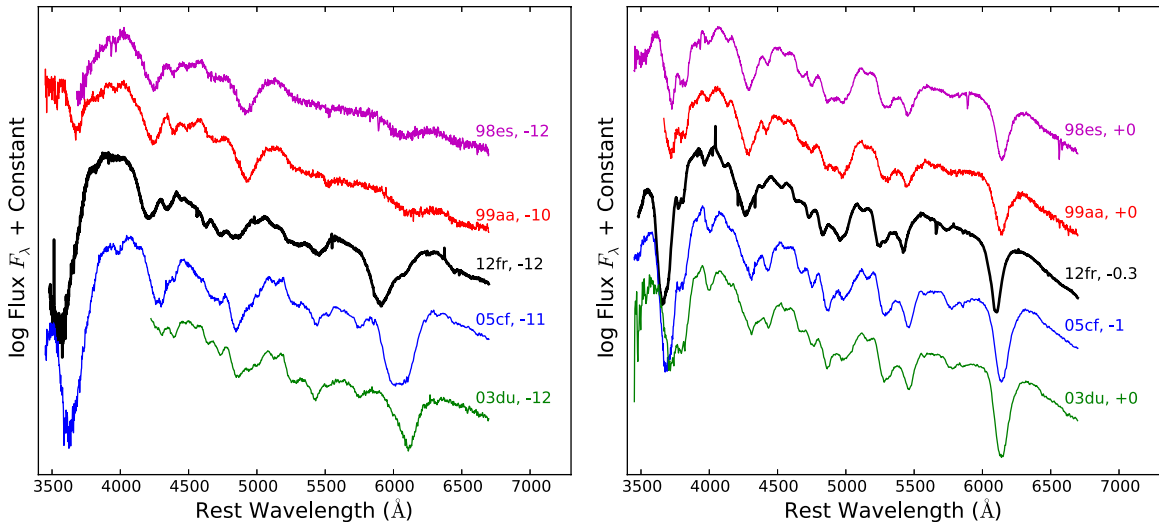
Figure 16. Spectrum of SN 2012fr compared to other SNe Ia at ∼12 days before maximum light (left) and at maximum light (right). Comparison SNe Ia are the SN 1991T-like SN 1998es (from Blondin et al. 2012), SN 1999aa (from Blondin et al. 2012), and the normal SNe Ia SN 2005cf (Wang et al. 2009b) and SN 2003du (Stanishev et al. 2007).

(A color version of this figure is available in the online journal.)

6.1. SN 2012fr and Velocity Evolution of Other SNe Ia

One of the most noteworthy features of the spectra of SN 2012fr was the extremely clear distinction between the low-velocity photospheric Si II $\lambda6355$ and an HVF. Clear identification of two absorption minima in the Si II $\lambda6355$ line has only been previously observed convincingly in SN 2009ig (Marion et al. 2013), but HVFs may manifest themselves more subtly in the line profiles of other SNe Ia. This may then have an impact on the measurement of the Si II $\lambda6355$ line velocity.

To inspect how common early HVF behavior is in SNe Ia, we searched for SNe Ia having spectra similar to the −10 day spectrum of SN 2012fr by employing the SN identification (SNID; Blondin & Tonry 2007) code. The top matches were, as expected, spectra of SNe Ia at about 10 days before maximum light, many of which exhibited a broad boxy absorption profile in the Si II $\lambda6355$ line. In Figure 17, we plot the Si II $\lambda6355$ profile of three notable matches—SN 2009ig (Foley et al. 2012; Marion et al. 2013), SN 2007le (from Blondin et al. 2012), and SN 2005cf (Wang et al. 2009b)—all of which exhibit an absorption-line profile that seems difficult to explain with a single component, either Gaussian or P-Cygni. The Si II $\lambda6355$ shape is best explained by a two-component profile like that observed in SN 2012fr, and this probability has been noted by previous authors (Mazzali 2001; Wang et al. 2009b; Foley et al. 2012).

A possible consequence of early HVFs in SNe Ia could be an overestimate of the velocity gradient in the Si II $\lambda6355$ line. To test this possibility, we convolved our spectra of SN 2012fr with a Gaussian filter of width $\sigma = 3500$ km s^{-1} (FWHM ≈ 6700 km s^{-1}) and measured the velocity minimum of the Si II $\lambda6355$ line. Several examples of the broadened spectra, along with the velocity evolution measured from these spectra, are shown in Figure 18. During the early epochs when the Si II $\lambda6355$ HVF is clearly distinct in the observed spectra, our convolved spectra show a single broad absorption feature whose velocity declines smoothly from ∼22,000 km s^{-1} to ∼12,000 km s^{-1} over about 6 days (velocities were almost exactly the pEW-weighted mean of the values from Table 2).
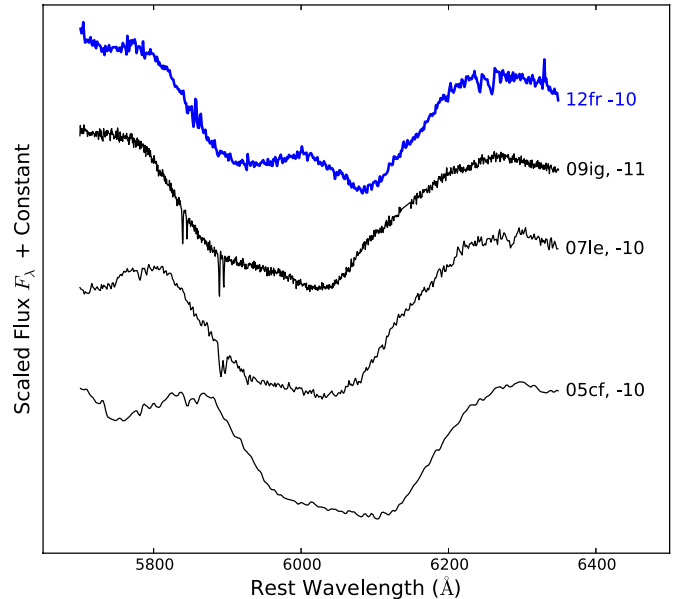
Figure 17. Si II $\lambda6355$ feature in the −10 day spectrum of SN 2012fr (blue) vs. early spectra of other SNe Ia with likely Si II $\lambda6355$ HVFs: SN 2009ig (Foley et al. 2012; Marion et al. 2013), SN 2007le (Blondin et al. 2012), and SN 2005cf (Wang et al. 2009b).

(A color version of this figure is available in the online journal.)

Though this implied velocity gradient is much higher than that observed in any other SNe Ia, it illustrates the fact that multiple distinct components blended in velocity space could masquerade as a single rapidly evolving component. Inspection of the shape of the Si II $\lambda6355$ absorption profile in HVG SNe Ia may provide insight into the possible impact of HVFs on the measured velocity gradients of these SNe.

Finally, we note that the long velocity plateau observed in SN 2012fr may not be unique, but instead may have been missed in other SNe Ia where the Si II $\lambda6355$ line is blended with the neighboring Fe lines at late times. Inspection of the full line complex in spectra later than +20 days (see Figure 1) shows that the mean wavelength of the absorption lines near
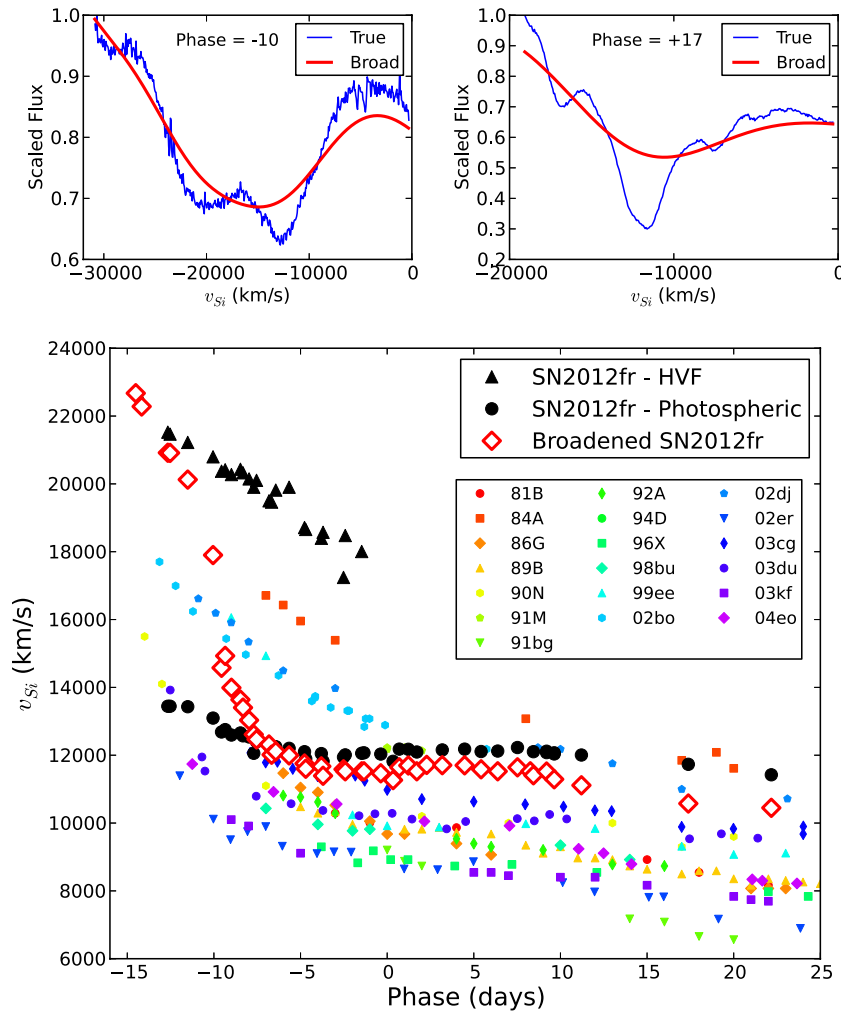
Figure 18. Top panels: observed spectra (blue) of SN 2012fr at -10 and $+17$ days, compared to spectra broadened by 3500 km^{-1} (red). Bottom: same as Figure 4, but with velocity measurements of the broadened SN 2012fr spectra shown as open red diamonds.

(A color version of this figure is available in the online journal.)

Si II λ6355 becomes redder, due to multiple Fe lines appearing to the red of Si II λ6355, while the individual lines remain at constant velocity. This behavior may be hidden in other SNe Ia having broader lines, or it may be misinterpreted as a decrease in the line velocity. Indeed, our test of the velocity-broadened spectra of SN 2012fr revealed a slight decrease in the broadened velocity minimum starting at about +10 days. Future modeling of the SN 2012fr spectra released here may be able to address this question in more detail by identifying the lines neighboring Si II λ6355 and how their relative strengths evolve with time.

6.2. The Nature of the SN 2012fr Explosion

The key observational features of SN 2012fr—long Si and Ca velocity plateau, narrow absorption features, and early HVFs—provide critical clues to the nature of its explosion. We will argue here that these observations indicate a thin region of partial burning products that produce the observed narrow line widths and IME velocity plateau, and which may be indicative of stratification in the ejecta. We then speculate on the origin of the HVFs, particularly in the context of recent proposals for surface He-shell burning.

6.2.1. Ejecta Stratification

The narrow velocity widths of the absorption profiles in SN 2012fr have enabled us to unambiguously track the velocity of the Si II λ6355 line to very late times, revealing a velocity plateau at $\sim$12,000 km s^{-1} until at least the final epoch of observation at +39 days. SNe Ia with such low velocity gradients have been observed before (e.g., the "LVG" subclass from Benetti et al. 2005). Notably, several SNe Ia have been found to exhibit a short-lived (i.e., few weeks duration) velocity plateau, such as the super-Chandrasekhar candidates presented by Scalzo et al. (2012), as well as SN 2005hj (Quimby et al. 2007) which also demonstrated a narrow velocity width.

The velocity plateaus for these other SNe Ia were explained in terms of explosion models featuring density enhancements at a particular velocity, which form at the reverse shock of an interaction between the SN ejecta and overlying material. Examples include "tamped detonations" and "pulsating delayed detonations," such as the DET2ENV and PDD series models of Khokhlov et al. (1993). In a tamped detonation, the SN ejecta interact with a compact envelope of H-poor material, such as the C–O envelope which might remain after a double-degenerate merger (Fryer et al. 2010; Shen et al. 2012); the interaction

freezes out quickly and the shock structure expands homologously thereafter. In a pulsating delayed detonation, the initial deflagration phase quenches and the WD progenitor undergoes a strong pulsation, causing the outer layers to contract. The contraction then reignites C and eventually results in a transition to a detonation, in which a shock forms at the interface between the expanding inner layers and contracting outer layers.

Regardless of how it forms, the dense layer in these models remains optically thick for some time, resulting in a plateau in the Si II velocity. Our analysis of Fe II lines in SN 2012fr, however, suggests that Si II detaches from the photosphere between day +8 and day +11, disfavoring a pure density enhancement as the cause of the Si II plateau in SN 2012fr. Additionally, in a tamped detonation, one would expect that material above the density-enhanced layer would correspond primarily to the unburned envelope; thus, the Si II HVF we observe in SN 2012fr is difficult to explain in this scenario.

Rather than indicating a pure density enhancement, the velocity plateau in Si II $\lambda6355$ may be evidence of Si II being confined to a narrow region in velocity space. This possibility is reinforced by the analogous velocity plateau in the Ca II IR triplet (Section 4.3.1) as well as the slightly lower velocity of the Fe II lines at late times (Section 4.4). This layering, along with the narrowness of the absorption features, indicates a probable stratification of the progress to complete nuclear burning in the ejecta. These properties are common in scenarios where the IMEs are produced mainly in a detonation phase (see, e.g., the recent work by Seitenzahl et al. 2013) as compared to deflagration scenarios, which result in significantly increased mixing in the ejecta.

Corroboration of stratification in the ejecta of SN 2012fr will be aided by nebular spectroscopy. Specifically, if the IMEs are distributed in a spherically symmetric shell, then these should manifest themselves as double-peaked nebular lines such as the argon lines astutely observed by Gerardy et al. (2007) in the mid-IR nebular spectrum of SN 2005df. Conversely, if the IMEs are distributed asymmetrically, as discerned from spectropolarimetric observations by Maund et al. (2013), then this may be revealed in asymmetry of the nebular IME line profile (unless, of course, the asymmetric geometry is not oriented favorably). However, IME nebular lines are challenging to observe, and most lines in nebular spectra arise from material burned to full nuclear statistical equilibrium (Fe and Ni). As Maund et al. (2013) note, a global asymmetry of SN 2012fr would produce velocity shifts of the nebular Fe lines, following the prediction of Maeda et al. (2010).

6.2.2. High-velocity Features

The HVFs in both Si and Ca also shed light on the nature of the SN 2012fr explosion. HVFs in the Ca II IR triplet appear to be a very common, perhaps even ubiquitous, feature in early-time SN Ia spectra (e.g., Mazzali et al. 2005a). HVFs in the Si II $\lambda6355$ line have also been observed in many SNe Ia (e.g., Wang et al. 2009b; Foley et al. 2012; Blondin et al. 2012; Silverman et al. 2012c; Marion et al. 2013). Positive identification of HVFs in other lines has been more challenging (though see Marion et al. 2013, for a thorough inspection of HVFs in multiple atomic species in SN 2009ig), so much effort has been focused on investigating the Ca II IR triplet and Si II $\lambda6355$ HVFs. Both the geometric distribution and the physical origin of the material responsible for these HVFs are active areas of investigation.

Tanaka et al. (2006) posited that the HVFs could be due to patches of material outside the nominal photosphere, and the relative strength of the photospheric and HVFs is due to the relative "covering fraction" of the outer layer of material. If the HVFs originated from patchy layers of material, they would likely lack spherical symmetry. Maund et al. (2013) recently presented spectropolarimetry of SN 2012fr and argued that the relatively high degree of polarization in the HVFs is inconsistent with spherically symmetric geometry. Such asymmetry in HVFs has been inferred from spectropolarimetry of other SNe Ia as well (for a review, see Wang & Wheeler 2008).

The physical origin of HVF material remains unclear. It has been suggested that HVFs could be due to CSM (Gerardy et al. 2004; Mazzali et al. 2005b), and for some SNe Ia CSM models have yielded favorable agreement with early-time SN Ia spectra with HVFs (Altavilla et al. 2007; Tanaka et al. 2008). In this scenario, absorption by Si II and Ca II may be enhanced if the CSM is partially enriched in H (CSM with $X(\mathrm{H}) < 0.3$ would not produce a detectable Hα feature; Tanaka et al. 2008), thereby favoring a lower ionization state for these ions. However, significant absorption by Ca and Si across a range of velocities in SN 2012fr is indicative of these features being produced by material in (or on) the WD that undergoes partial nuclear burning during (or prior to) the SN explosion.

A possible explanation for the HVFs in SN 2012fr may be the detonation of He-rich material at the surface of the exploding WD. If an He layer of sufficiently low density is consumed by a detonation, then the low density prevents burning to Fe-group elements but can be sufficient to produce Si and Ca (K. Nomoto 2012, private communication). In the single-degenerate Chandrasekhar-mass scenario, an He layer may be present following accretion from a binary companion. Explosive burning in a surface He layer is also a generic feature in the double-detonation scenario (Fink et al. 2007, 2010; Kromer et al. 2010; Sim et al. 2010, 2012), where the detonation of the He layer induces a detonation near the core of the WD progenitor, and even in merger scenarios in which the CO WDs retain a small He-rich atmosphere (R. Pakmor 2012, private communication). Recent work by Townsley et al. (2012) showed that He-shell burning could produce significant amounts of Ca, especially if the surface layer dredges up C from the WD surface through convection. However, one drawback of the He-shell scenario is that significant amounts of unburned He remain in most simulations, and while the remaining He should produce clear signatures in SN Ia spectra (Mazzali & Lucy 1998), these features are not actually observed in SNe Ia.

Another possibility is that Si and Ca abundances are enhanced in the outer layers of a WD due to surface He burning that occurred prior to the SN event. This might arise during a surface He flash (e.g., Nomoto et al. 2013) that manifests itself as a recurrent nova. This He-shell flash could produce relatively high Si and Ca abundances in the outer layers of the WD, or it might also ejecta partial burning products. These could either fall back onto the surface of the WD (again providing enrichment of the outer WD layers prior to explosion), or perhaps enrich part of the CSM into which the SN ejecta subsequently expand, and in principle the ejected material might be directly detected as CSM interaction of the SN (e.g., as in PTF11kx; Dilday et al. 2012).

Thus, it is difficult at this time to constrain the exact origin of HVFs in SNe Ia, including SN 2012fr, but our data provide important observational constraints. HVFs in both Si II $\lambda6355$ and the Ca II IR triplet were observed from two weeks before maximum light until they faded to obscurity at roughly -2 and $+10$ days, respectively. These HVFs were cleanly distinguished from the thin photospheric shell and showed strong velocity

Table 7
Spectroscopic Classes of H_0 Fundamental Calibrators

SN	Host	d^a (Mpc)	$\Delta m_{15}(B)$ (mag)	pEW(5972) (Å)	pEW(6355) (Å)	v_{Si} (km s^{-1})	Branch Class	Wang Class	References
SN 1981B	NGC 4536	14.8	1.07 ± 0.09	20.0	129.0	13754	BL	HV	1, 2, 3
SN 1990N	NGC 4639	21.6	1.00 ± 0.03	10.9	87.1	9352	CN	N	4, 5
SN 1994ae	NGC 3370	26.6	0.96 ± 0.04	7.4	81.6	10979	CN	N	5
SN 1995al	NGC 3021	30.5	0.87 ± 0.04	15.0	112.9	12149	BL	HV	5
SN 1998aq	NGC 3982	22.5	1.11 ± 0.04	11.1	77.1	10796	CN	N	5
SN 2002fk	NGC 1309	32.5	1.13 ± 0.03	10.3	75.7	10057	CN	N	5
SN 2007af	NGC 5584	22.4	1.04 ± 0.01	17.0	105.2	10969	BL	N	5
SN 2007sr	NGC 4038	21.7	1.13 ± 0.06	. . .	. . .	. . .	. . .	. . .	6
SN 1998dh	NGC 7541	36.7	1.17 ± 0.06	10.1	121.8	12091	BL	HV	5
SN 2001el	NGC 1448	15.9	1.13 ± 0.04	12.0	93.0	11321	CN	N	7, 8
SN 2003du	UGC 9391	26.1	1.07 ± 0.06	1.9	88.8	10527	CN	N	5, 9
SN 2005cf	MCG −01-39-3^b	26.4	1.05 ± 0.03	6.5	99.1	10352	CN	N	10, 5
SN 2006D	MCG −01-33-34	34.9	1.35 ± 0.05	21.4	94.4	10833	CN	N	5
SN 2009ig	NGC 1015	35.9	0.89 ± 0.02	4.7	79.9	13400	CN	HV	11, 12, 5
SN 2011fe	M101	6.7	1.07 ± 0.06	15.1	101.4	10331	CN	N	13, 14
SN 2012fr	NGC 1365	17.9	0.80 ± 0.01	3.9	66.5	12037	SS/CN	HV/N	. . .

Notes.
[a] Distances from Cepheids for the Riess et al. (2011) sample, Kennicutt et al. (1998) and Freedman et al. (2001) for M101, Silbermann et al. (1999) and Freedman et al. (2001) for NGC 1365, and redshift using $H_0 = 73.8$ km s^{-1} Mpc^{-1} for others.
[b] Tidal bridge between MCG −01-39-3 and MCG −01-39-2 (NGC 5917); see Wang et al. (2009b).
References. (1) Schaefer 1995; (2) Branch et al. 1983; (3) Branch et al. 2009; (4) Ganeshalingam et al. 2010; (5) Blondin et al. 2012; (6) Hicken et al. 2012; (7) Krisciunas et al. 2003; (8) Wang et al. 2003; (9) Stanishev et al. 2007; (10) Wang et al. 2009b; (11) Foley et al. 2012; (12) Marion et al. 2013; (13) Vinkó et al. 2012; (14) Parrent et al. 2012.

gradients consistent with a receding photosphere. The velocity and absorption-strength evolution of these HVFs, along with the geometry implied from spectropolarimetry (Maund et al. 2013), provide important constraints for any model which posits an explanation for these features.

6.3. SN 2012fr and the Hubble Constant

SN 2012fr occurred in NGC 1365, one of the galaxies included in the *HST* Key Project on the extragalactic distance scale (Freedman et al. 2001; Silbermann et al. 1999). This fortuitous situation has made it a leading candidate to contribute toward measurement of the peak luminosity of SNe Ia. Such information is critical for determining the Hubble constant, and in the recent H_0 measurement by Riess et al. (2011), only eight SNe Ia with good light curves had independent distance measurements from observations of Cepheid variable stars in their host galaxies. Due to the existing Cepheid data for NGC 1365, SN 2012fr stands poised to be added to this sample. Because much of the effort in studying potential spectroscopic subclasses of SNe Ia has been aimed at improving the standardization of their luminosities, it is valuable to investigate where the fundamental calibrator SNe Ia sit in this context. Thus, in this section, we inspect where the existing and probable future members of the Hubble-constant sample, including SN 2012fr, reside in the new SN Ia spectroscopic classification schemes.

In Table 7, we summarize the light-curve decline rate and spectroscopic indicator data for the current sample of H_0 calibrators from Riess et al. (2011), as well as a sample of seven additional SNe Ia that are strong candidates to be added to the H_0 sample, along with SN 2012fr. Selection criteria for the "likely" sample include (1) low reddening of the SN from its host, i.e., $A_V \lesssim 0.5$ mag; (2) high sampling of the SN light curve including pre-maximum data; (3) no spectroscopic peculiarity of the SN; (4) distance modulus of the host of $\mu \lesssim 32.8$ mag; and

(5) sufficiently low inclination to avoid crowding of Cepheids (L. Macri & A. Riess 2012, private communication). The seven new SNe Ia which likely satisfy the above criteria are SN 1998dh, SN 2001el, SN 2003du, SN 2005cf, SN 2006D, SN 2009ig, and SN 2011fe.

We note here that for our selection criteria, spectroscopic peculiarity is explicitly defined as similarity to the peculiar SN Ia subclasses defined by their respective prototypes SN 1991bg, SN 1991T, SN 1999aa, and SN 2002cx. While SN 2012fr exhibits some rare behaviors, such as very narrow lines and a late velocity plateau in the IMEs, these characteristics are all seen in other SNe Ia (though not previously in this combination). Most importantly, the composition of SN 2012fr inferred from its spectral features is consistent with that of normal SNe Ia (see Figure 16), and the more subtle characteristics of its absorption features fall within the range of typical SN Ia behavior.

In Figure 19, we plot the location of existing and likely future H_0 calibrator SNe Ia along with SN 2012fr and the same comparison sample from Figure 15. The H_0 calibrator sample is not composed exclusively of SNe Ia falling in the "core normal" spectroscopic class of Branch et al. (2009) or the "normal" velocity class of Wang et al. (2009a). SN 2012fr would have the slowest light-curve decline rate and shallowest Si absorption of the H_0 sample, but not the highest velocity. This prompts the question of what degree of "normality" is required for an SN Ia to be used for cosmology. The answer will likely require further study of SN Ia spectroscopic diversity and its impact on SN Ia luminosities.

7. CONCLUSIONS

We present optical spectra of SN 2012fr, a relatively normal SN Ia that exhibits several interesting features. These include the distinct presence of HVFs in both the Si II λ6355 line and the Ca II IR triplet, as well as a long-lived velocity plateau at late epochs in both lines. These behaviors were made
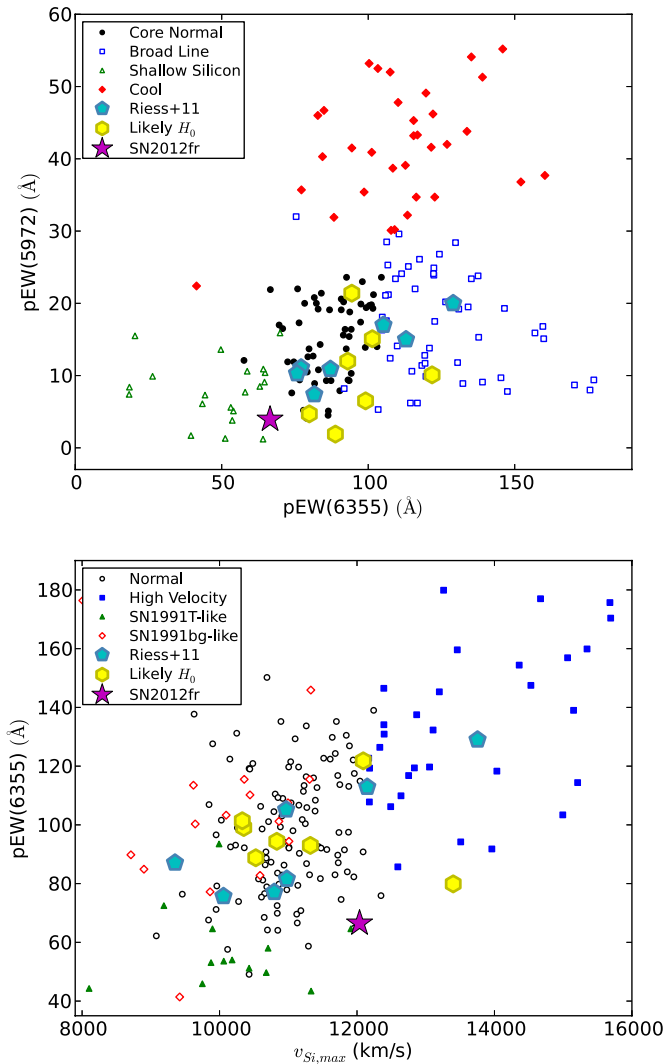
Figure 19. Current members of the H_0 fundamental calibrator sample (cyan pentagons) and likely new additions to the sample (yellow hexagons), along with SN 2012fr (purple star), compared to other SNe Ia on the Branch et al. (2009) diagram (top) and the Wang et al. (2009a) diagram (bottom). Other SN Ia subclasses are denoted as in Figure 15.

(A color version of this figure is available in the online journal.)

more clear by the extremely narrow velocity width of the photospheric absorption-line profiles. We show that SN 2012fr has Si II velocities and absorption strengths that place it near the boundary between the "shallow silicon" and "core normal" spectroscopic classes defined by Branch et al. (2009), and on the boundary between normal and "HV" SNe Ia as defined by Wang et al. (2009a).

SN 2012fr exhibits a very slow decline rate ($\Delta m_{15}(B) = 0.80 \pm 0.01$ mag; see Paper II), relatively shallow Si absorption at maximum light (pEW(6355) = 66.5 ± 15.5 Å), and a very low velocity gradient ($\dot{v} = 0.3 \pm 10.0$ km s^{-1} day^{-1}). All of these characteristics are common in the very luminous SN 1991T-like and SN 1999aa-like SN Ia subclasses, but SN 2012fr has higher ejecta velocities and much stronger Si and Ca absorption at early epochs than most SNe Ia in these classes (see Figure 16). Thus, SN 2012fr likely represents the most luminous end of the normal SN Ia spectrum, and it may be a transitional object between normal and very luminous events.

In the modern era, only three well-observed normal SNe Ia (SN 1981B, SN 2001el, and SN 2011fe) have occurred in galaxies that are both suitable for Cepheid distances and closer than the host galaxy of SN 2012fr, NGC 1365. Furthermore, this galaxy has been extensively studied and was part of the *HST* Key Project on the extragalactic distance scale. This makes SN 2012fr a prime candidate for measuring the peak luminosity of SNe Ia and thereby constraining the Hubble constant, and we show that SN 2012fr should provide an excellent complement to the existing and likely future sample of H_0 SNe Ia.

Individual SNe Ia such as SN 2012fr with extensive observational data sets can prove invaluable for better understanding the nature of SN Ia explosions. Here we already identify a number of tantalizing observational characteristics of this spectral time series, and we expect that future detailed modeling could reveal additional subtle insights.

REFERENCES

Altavilla, G., Stehle, M., Ruiz-Lapuente, P., et al. 2007, A&A, 475, 585
Benetti, S., Cappellaro, E., Mazzali, P. A., et al. 2005, ApJ, 623, 1011
Benetti, S., Meikle, P., Stehle, M., et al. 2004, MNRAS, 348, 261
Blondin, S., Matheson, T., Kirshner, R. P., et al. 2012, AJ, 143, 126
Blondin, S., & Tonry, J. L. 2007, ApJ, 666, 1024
Bongard, S., Baron, E., Smadja, G., Branch, D., & Hauschildt, P. H. 2006, ApJ, 647, 513
Branch, D., Dang, L. C., & Baron, E. 2009, PASP, 121, 238
Branch, D., Lacy, C. H., McCall, M. L., et al. 1983, ApJ, 270, 123
Branch, D., Thomas, R. C., Baron, E., et al. 2004, ApJ, 606, 413
Buil, C. 2012, CBET, 3275, 3
Bureau, M., Mould, J. R., & Staveley-Smith, L. 1996, ApJ, 463, 60
Buzzoni, B., Delabre, B., Dekker, H., et al. 1984, Msngr, 38, 9
Childress, M., Zhou, G., Tucker, B., et al. 2012, CBET, 3275, 2
Chotard, N., Gangler, E., Aldering, G., et al. 2011, A&A, 529, L4
Crawford, S. M., Still, M., Schellart, P., et al. 2010, Proc. SPIE, 7737, 773725
Dilday, B., Howell, D. A., Cenko, S. B., et al. 2012, Sci, 337, 942
Dopita, M., Hart, J., McGregor, P., et al. 2007, Ap&SS, 310, 255
Dopita, M., Rhee, J., Farage, C., et al. 2010, Ap&SS, 327, 245
Dressler, A., Bigelow, B., Hare, T., et al. 2011, PASP, 123, 288
Filippenko, A. V., Richmond, M. W., Matheson, T., et al. 1992, ApJL, 384, L15
Fink, M., Hillebrandt, W., & Röpke, F. K. 2007, A&A, 476, 1133
Fink, M., Röpke, F. K., Hillebrandt, W., et al. 2010, A&A, 514, A53
Folatelli, G., Phillips, M. M., Morrell, N., et al. 2012, ApJ, 745, 74
Foley, R. J. 2012, arXiv:1212.6261
Foley, R. J., Challis, P. J., Filippenko, A. V., et al. 2012, ApJ, 744, 38
Foley, R. J., Papenkova, M. S., Swift, B. J., et al. 2003, PASP, 115, 1220
Foley, R. J., Sanders, N. E., & Kirshner, R. P. 2011, ApJ, 742, 89
Freedman, W. L., Madore, B. F., Gibson, B. K., et al. 2001, ApJ, 553, 47
Fryer, C. L., Ruiter, A. J., Belczynski, K., et al. 2010, ApJ, 725, 296
Ganeshalingam, M., Li, W., Filippenko, A. V., et al. 2010, ApJS, 190, 418
Garavini, G., Folatelli, G., Goobar, A., et al. 2004, AJ, 128, 387
Gerardy, C. L., Höflich, P., Fesen, R. A., et al. 2004, ApJ, 607, 391
Gerardy, C. L., Meikle, W. P. S., Kotak, R., et al. 2007, ApJ, 661, 995
Hamuy, M., Folatelli, G., Morrell, N. I., et al. 2006, PASP, 118, 2
Hicken, M., Challis, P., Kirshner, R. P., et al. 2012, ApJS, 200, 12
Hoeflich, P., & Khokhlov, A. 1996, ApJ, 457, 500
Hoyle, F., & Fowler, W. A. 1960, ApJ, 132, 565
Hsiao, E. Y., Marion, G. H., Phillips, M. M., et al. 2013, ApJ, 766, 72
Iben, I., Jr., & Tutukov, A. V. 1984, ApJS, 54, 335
Kennicutt, R. C., Jr., Stetson, P. B., Saha, A., et al. 1998, ApJ, 498, 181
Khokhlov, A., Mueller, E., & Hoeflich, P. 1993, A&A, 270, 223
Klotz, A., Normand, J., Conseil, E., et al. 2012, CBET, 3276, 1
Krisciunas, K., Suntzeff, N. B., Candia, P., et al. 2003, AJ, 125, 166
Kromer, M., Sim, S. A., Fink, M., et al. 2010, ApJ, 719, 1067
Li, W., Bloom, J. S., Podsiadlowski, P., et al. 2011, Natur, 480, 348

Li, W., Filippenko, A. V., Treffers, R. R., et al. 2001, ApJ, 546, 734
Maeda, K., Benetti, S., Stritzinger, M., et al. 2010, Natur, 466, 82
Maguire, K., Sullivan, M., Ellis, R. S., et al. 2012, MNRAS, 426, 2359
Marion, G. H., Vinko, J., Wheeler, J. C., et al. 2013, arXiv:1302.3537
Matheson, T., Kirshner, R. P., Challis, P., et al. 2008, AJ, 135, 1598
Maund, J. R., Spyromilio, J., Hoeflich, P. A., et al. 2013, arXiv:1302.0166
Mazzali, P. A. 2001, MNRAS, 321, 341
Mazzali, P. A., Benetti, S., Altavilla, G., et al. 2005a, ApJL, 623, L37
Mazzali, P. A., Benetti, S., Stehle, M., et al. 2005b, MNRAS, 357, 200
Mazzali, P. A., & Lucy, L. B. 1998, MNRAS, 295, 428
Mazzali, P. A., Nomoto, K., Cappellaro, E., et al. 2001, ApJ, 547, 988
Mazzali, P. A., Röpke, F. K., Benetti, S., & Hillebrandt, W. 2007, Sci, 315, 825
Miller, J. S., & Stone, R. P. S. 1993, Lick Obs. Tech. Rep. 66 (Santa Cruz, CA: Lick Obs.)
Moorwood, A., Cuby, J.-G., & Lidman, C. 1998, Msngr, 91, 9
Nomoto, K., Kamiya, Y., & Nakasato, N. 2013, in IAU Symp. 281, Binary Paths to Type Ia Supernovae Explosions, ed. R. Di Stefano, M. Orio, & M. Moe (Cambridge: Cambridge Univ. Press), 253
Nugent, P., Phillips, M., Baron, E., Branch, D., & Hauschildt, P. 1995, ApJL, 455, L147
Nugent, P. E., Sullivan, M., Cenko, S. B., et al. 2011, Natur, 480, 344
Parrent, J. T., Howell, D. A., Friesen, B., et al. 2012, ApJL, 752, L26
Parrent, J. T., Thomas, R. C., Fesen, R. A., et al. 2011, ApJ, 732, 30
Patat, F., Chandra, P., Chevalier, R., et al. 2007, Sci, 317, 924
Perlmutter, S., Aldering, G., Goldhaber, G., et al. 1999, ApJ, 517, 565
Phillips, M. M. 1993, ApJL, 413, L105
Phillips, M. M., Lira, P., Suntzeff, N. B., et al. 1999, AJ, 118, 1766
Phillips, M. M., Wells, L. A., Suntzeff, N. B., et al. 1992, AJ, 103, 1632
Pinto, P. A., & Eastman, R. G. 2000, ApJ, 530, 757
Poznanski, D., Ganeshalingam, M., Silverman, J. M., & Filippenko, A. V. 2011, MNRAS, 415, L81
Poznanski, D., Prochaska, J. X., & Bloom, J. S. 2012, MNRAS, 426, 1465
Quimby, R., Höflich, P., & Wheeler, J. C. 2007, ApJ, 666, 1083
Riess, A. G., Filippenko, A. V., Challis, P., et al. 1998, AJ, 116, 1009
Riess, A. G., Macri, L., Casertano, S., et al. 2011, ApJ, 730, 119
Scalzo, R., Aldering, G., Antilogus, P., et al. 2012, ApJ, 757, 12
Schaefer, B. E. 1995, ApJL, 449, L9
Schlafly, E. F., & Finkbeiner, D. P. 2011, ApJ, 737, 103
Seitenzahl, I. R., Ciaraldi-Schoolmann, F., Röpke, F. K., et al. 2013, MNRAS, 429, 1156
Shen, K. J., Bildsten, L., Kasen, D., & Quataert, E. 2012, ApJ, 748, 35
Silbermann, N. A., Harding, P., Ferrarese, L., et al. 1999, ApJ, 515, 1
Silverman, J. M., & Filippenko, A. V. 2012, MNRAS, 425, 1917
Silverman, J. M., Foley, R. J., Filippenko, A. V., et al. 2012a, MNRAS, 425, 1789
Silverman, J. M., Ganeshalingam, M., Cenko, S. B., et al. 2012b, ApJL, 756, L7
Silverman, J. M., Kong, J. J., & Filippenko, A. V. 2012c, MNRAS, 425, 1819
Sim, S. A., Fink, M., Kromer, M., et al. 2012, MNRAS, 420, 3003
Sim, S. A., Röpke, F. K., Hillebrandt, W., et al. 2010, ApJL, 714, L52
Simon, J. D., Gal-Yam, A., Gnat, O., et al. 2009, ApJ, 702, 1157
Stanishev, V., Goobar, A., Benetti, S., et al. 2007, A&A, 469, 645
Stehle, M., Mazzali, P. A., Benetti, S., & Hillebrandt, W. 2005, MNRAS, 360, 1231
Sternberg, A., Gal-Yam, A., Simon, J. D., et al. 2011, Sci, 333, 856
Tanaka, M., Mazzali, P. A., Benetti, S., et al. 2008, ApJ, 677, 448
Tanaka, M., Mazzali, P. A., Maeda, K., & Nomoto, K. 2006, ApJ, 645, 470
Thomas, R. C., Aldering, G., Antilogus, P., et al. 2007, ApJL, 654, L53
Thomas, R. C., Aldering, G., Antilogus, P., et al. 2011a, ApJ, 743, 27
Thomas, R. C., Nugent, P. E., & Meza, J. C. 2011b, PASP, 123, 237
Townsley, D. M., Moore, K., & Bildsten, L. 2012, ApJ, 755, 4
Tutukov, A. V., & Iungelson, L. R. 1976, Afz, 12, 521
Tutukov, A. V., & Yungelson, L. R. 1979, AcA, 29, 665
van Rossum, D. R. 2012, arXiv:1208.3781
Vinkó, J., Sárneczky, K., Takáts, K., et al. 2012, A&A, 546, A12
Vogt, S. S., Allen, S. L., Bigelow, B. C., et al. 1994, Proc. SPIE, 2198, 362
Wang, L., Baade, D., Höflich, P., et al. 2003, ApJ, 591, 1110
Wang, L., & Wheeler, J. C. 2008, ARA&A, 46, 433
Wang, X., Filippenko, A. V., Ganeshalingam, M., et al. 2009a, ApJL, 699, L139
Wang, X., Li, W., Filippenko, A. V., et al. 2009b, ApJ, 697, 380
Webbink, R. F. 1984, ApJ, 277, 355
Whelan, J., & Iben, I., Jr. 1973, ApJ, 186, 1007
Wiese, W. L., Smith, M. W., & Miles, B. M. 1969, Atomic Transition Probabilities. Vol. 2: Sodium through Calcium. A Critical Data Compilation (Washington, DC: National Bureau of Standards)
Yaron, O., & Gal-Yam, A. 2012, PASP, 124, 668